

1 **Wind-driven interannual variability of sea ice algal production**  
2 **in the western Arctic Chukchi Borderland**

3  
4 **Eiji Watanabe\*<sup>1</sup>, Jonaotaro Onodera<sup>1</sup>, Naomi Harada<sup>1</sup>,**  
5 **Maki Noguchi Aita<sup>1</sup>, Akio Ishida<sup>2</sup>, and Michio J. Kishi<sup>3</sup>**

6  
7 *<sup>1</sup>Japan Agency for Marine-Earth Science and Technology, Yokosuka, Japan*

8 *2-15 Natsushima, Yokosuka, Kanagawa, 237-0061, JAPAN*

9 *Tel: +81-46-867-9480*

10 *E-mail: ejnabe@jamstec.go.jp*

11  
12 *<sup>2</sup>Department of Social and Environmental Studies, Tokoha University, Fuji, Japan*

13 *<sup>3</sup>Faculty of Fisheries Sciences, Hokkaido University, Hakodate, Japan*

14

15 **Abstract**

16 Seasonal and interannual variability in the biogenic particle sinking flux was recorded  
17 using multi-year bottom-tethered sediment trap mooring systems in the Northwind Abyssal  
18 Plain (Station NAP: 75°N, 162°W, 1975-m water depth) of the western Arctic Chukchi  
19 Borderland. Trapped particle flux at a median depth of 184 m had an obvious peak and  
20 dominance of sea ice-related diatom assemblages in August 2011. The observed particle flux  
21 was considerably suppressed throughout summer 2012. In the present study, the response of ice  
22 algal production and biomass to wind-driven changes in the physical environment was  
23 addressed using a pan-Arctic sea ice-ocean modeling approach. A sea ice ecosystem with ice  
24 algae was newly incorporated into the lower-trophic marine ecosystem model, which was  
25 previously coupled with a high-resolution (i.e., 5-km horizontal grid size) sea ice-ocean general  
26 circulation model. Seasonal model experiments covering two-year mooring periods indicated  
27 that primary productivity of ice algae around the Chukchi Borderland depended on basin-scale  
28 wind patterns via various processes. Easterly winds in the southern part of a distinct Beaufort  
29 High supplied nutrient-rich water for euphotic zones of the NAP region via both surface Ekman  
30 transport of Chukchi shelf water and vertical turbulent mixing with underlying nutricline water  
31 in 2011. In contrast, northwesterly winds flowing in the northern part of an extended Siberian  
32 High transported oligotrophic water within the Beaufort Gyre circulation toward the NAP  
33 region in 2012. The modeled ice algal biomass during summer reflected the differences in  
34 nutrient distribution. The modeled sinking flux of particulate organic nitrogen (PON) was  
35 comparable with the time series obtained from sediment trap data in summer 2011. In contrast,  
36 lateral advection of ice algal patches of shelf origin during a great cyclone event may have  
37 caused a modeled PON flux bias in 2012. Sensitivity experiments revealed several uncertainties

38 of model configurations of ice algal productivity, particle sinking speed, and grazing activities.  
39 Extending the year-long measurements is expected to help illustrate the more general features  
40 of ice-related biological processes in the Arctic Ocean.  
41 **Keywords:** Arctic Ocean, Northwind Abyssal Plain, ice algae model, primary production, wind pattern

## 42 **1. Introduction**

43 The response of biogeochemical cycles to the decline in Arctic sea ice has become an  
44 important topic for a variety of communities. Improved light conditions during summer have  
45 enhanced phytoplankton photosynthesis activity in the Eurasian pelagic area of the Arctic  
46 Ocean (Wassmann, 2011). A widespread massive deposition of ice algal biomass was detected  
47 on the deep seafloor of the eastern Arctic basin (Boetius et al., 2013). On the other hand, the  
48 under-ice export of particulate organic carbon (POC) was limited by insufficient nutrient supply  
49 in the stratified central Arctic (Lalande et al., 2014). In the Beaufort Gyre region of the western  
50 Arctic, freshwater accumulation suppressed primary production during the 2000s (McLaughlin  
51 et al., 2010; Nishino et al., 2011). It is necessary to fill in the observational gaps to understand  
52 spatial and temporal variability in the biological processes of the Arctic Ocean.

53 Sediment trap measurements are useful to capture year-long biological activity signals. The  
54 locations of bottom-tethered traps have been confined to the north of the Laptev Sea (Fahl and  
55 Nöthig, 2007), Mackenzie shelf (Forest et al., 2007), and the deep Canada Basin (Honjo et al.,  
56 2010; Hwang et al., 2015). In our field campaign, year-round bottom-tethered moorings,  
57 including sediment trap instruments, have been deployed in the Northwind Abyssal Plain  
58 (NAP) of the Chukchi Borderland since October 2010 (Fig. 1). Early-winter maxima of sinking  
59 particle flux with fresh organic material have been captured annually at Station NAP (75°N,  
60 162°W, 1,975 m water depth) (Watanabe et al., 2014; Onodera et al., 2015). The substantial  
61 quantities of lithogenic minerals in the trapped particles suggest shelf-origin water transport  
62 toward the NAP region. Seasonal experiments using an eddy-resolving (5 km grid size) pan-  
63 Arctic sea ice-ocean model indicated the effective role of Beaufort shelf-break eddies in the  
64 transport of Chukchi shelf water with high biological productivity and in the consequent early-

65 winter peaks of sinking biogenic flux at Station NAP (Watanabe et al., 2014). It should be noted  
66 that biological production continued inside these eddies moving in the southern Canada Basin.

67 Another finding obtained at Station NAP was remarkable interannual variability in summer  
68 particle flux (Onodera et al., 2015; Ikenoue et al. 2015; Matsuno et al., 2015). Trapped particle  
69 flux peaked sharply in August 2011 but was suppressed considerably during summer 2012. The  
70 diatom assemblage compositions suggest that year-to-year changes in the distribution of shelf-  
71 origin water and relatively oligotrophic water originating from the interior of the Canada Basin  
72 controls the particle flux around the Chukchi Borderland (Onodera et al., 2015). This situation  
73 was supported by ocean current fields simulated in a medium-resolution (25 km grid size)  
74 framework by the pan-Arctic physical oceanographic model (Onodera et al., 2015). However,  
75 reliable *in-situ* biological productivity and water mass transport data above the shallow trap  
76 depth (approximately 180–260 m) was not available at Station NAP during the mooring periods  
77 (October 2010–September 2012). In particular, chlorophyll, nutrient concentration, and ocean  
78 velocity data from winter to early summer were insufficient. Further detailed investigation of  
79 the background mechanisms associated with summer biogenic flux would be highly valuable  
80 and possible using a coupled physical and marine ecosystem model. Whereas the main content  
81 of observed diatom valves was the sea ice-related species (e.g., *Fossula arctica*, Onodera et al.,  
82 2015), the sea ice ecosystem was not included in our previous model experiment (Watanabe et  
83 al., 2014). The lack of ice algae was a plausible factor for the summer delay of the simulated  
84 biogenic flux peak behind the trap data. These issues raised our motivation to incorporate ice-  
85 related biogeochemical processes in the model.

86 Ice algae models have a long history of development. Pioneering work was conducted on  
87 the Antarctic fast ice ecosystem (Arrigo et al., 1993). For the Arctic Ocean, one-dimensional ice

88 algae models were applied to landfast ice in Resolute Passage of the Canadian Archipelago  
89 (Lavoie et al., 2005; Pogson et al., 2011) and offshore Barrow (Jin et al., 2006). The modeled  
90 region has been extended in recent years to include the entire Arctic Ocean (Dupont, 2012) and  
91 global domain (Deal et al., 2011; Jin et al., 2012). The analysis period covered seasonal  
92 transition (Lavoie, 2005; Deal et al., 2011) to decadal variability (Jin et al., 2012; Dupont,  
93 2012) and future projections (Lavoie et al., 2010). Most models assume that ice algal activity  
94 occurs primarily in the skeletal layer of the sea ice bottom (i.e., ice-water interface), where the  
95 layer thickness is fixed at 2 cm (Lavoie et al., 2005), 3 cm (Jin et al., 2012), and 5 cm (Dupont,  
96 2012). The ice algal biomass sometimes reaches values three orders of magnitude larger at the  
97 ice-water interface than that in the upper part of the sea ice column (e.g., Jin et al., 2006).  
98 Ocean surface water is a major nutrient supplier for ice algae in the skeletal layer. Tidal mixing  
99 controls nutrient exchange rates at the ice-water interface in the narrow shallow straits of the  
100 Canadian Archipelago (Lavoie et al., 2005). In a general viewpoint, it is reasonable that nutrient  
101 flux is calculated as a function of the sea ice freezing/melting rate (Arrigo et al., 1993; Jin et al.,  
102 2006). However, Dupont (2012) did not calculate nutrient import due to sea ice freezing,  
103 following an observational view where nutrients trapped inside the sea ice column have minor  
104 contributions to an ice algal bloom (Cota et al., 1991; Cota and Smith, 1991). As grazing  
105 pressure on ice algae is considered weak in the sea ice column, most previous models excluded  
106 zooplankton biology in the skeletal layer (Jin et al., 2006; Dupont, 2012) or prescribed a small  
107 grazing rate to potential grazers (e.g., amphipods) (Lavoie, 2005). The habitat of ice algae in the  
108 skeletal layer disappears gradually due to melting sea ice. The assemblages released from the  
109 sea ice bottom partially act as phytoplankton and become a food source for pelagic grazers in

110 the water column (Michel et al., 1993, 1996). Thus, complex ice algal processes have been  
111 proposed and numerically formulated in various ways.

112 In the present study, seasonal and interannual variability of ice algal production and  
113 biomass in the Chukchi Borderland were addressed using a pan-Arctic sea ice-ocean modeling  
114 approach (Fig. 1). We focused particularly on the relationships between ice-related  
115 biogeochemical processes and wind-driven dynamics, such as shelf-basin exchanges, local  
116 upwelling/downwelling, and vertical turbulent mixing. To represent the summer biogenic  
117 particle flux captured by sediment trap measurements, the simple sea ice ecosystem was newly  
118 incorporated into a lower-trophic marine ecosystem model. Our model coupled with a  
119 sophisticated high-resolution physical component is a powerful tool for the above-mentioned  
120 subjects because of following issues. The Chukchi Borderland is composed of complex  
121 topography such as long ridges, deep-sea plateaus, and steep shelf breaks. The sinking biogenic  
122 flux available for comparison was obtained from the single-point mooring measurements in this  
123 area. The source regions of surface water are distributed over the Chukchi Sea, the East  
124 Siberian Sea, and the Canada Basin. The water mass transports are closely related to shelf-basin  
125 boundary currents and baroclinic eddies. These complex topography and mesoscale  
126 hydrographic features have been unresolved by previous basin-scale ice algae models, which  
127 horizontal resolution was much coarser than the typical internal Rossby radius of deformation  
128 (ca. 10 km) in the polar region (Zhao et al., 2014). The linkages between wind patterns, light  
129 and nutrient preconditioning of ice algal bloom, and particle sinking are also unique viewpoints  
130 in the present work. Modeling configurations and sediment trap analyses are described in  
131 Section 2. Seasonal transitions of the modeled ice-ocean field, particularly those around the  
132 NAP region, are traced in Section 3. Relationships between the interannual variability in

133 biogeochemical properties and wind patterns are examined in Section 4. Uncertainties of the  
134 modeled processes are discussed in Section 5, based on sensitivity experiments. The obtained  
135 findings are summarized in Section 6.  
136



## 137 **2. Model configuration and experimental design**

### 138 **2.1 Physical oceanographic model**

139 The physical part of the coupled sea ice-ocean model is the “Center for Climate System  
140 Research Ocean Component Model (COCO)” version 4.9 (Hasumi, 2006). The sea ice  
141 component includes a multi-thickness-category configuration based on that of Bitz et al. (2001)  
142 with a one-layer thermodynamic formulation (Bitz and Lipscomb, 1999), the linear-remapping  
143 method for category transfer (Lipscomb, 2001), and the elastic-viscous-plastic rheology (Hunke  
144 and Dukowicz, 1997). In addition to the open water category, the lower limit of sea ice  
145 thickness in each category is set to 10, 30, 60, 100, 250, and 500 cm, respectively (i.e., 7  
146 categories). The ocean component is a free-surface general circulation model formulated using  
147 the advection scheme of Leonard et al. (1994) and the turbulence closure mixed-layer scheme  
148 of Noh and Kim (1999).

149

### 150 **2.2 Marine ecosystem model**

151 The COCO model was coupled with a lower-trophic marine ecosystem model, “North  
152 Pacific Ecosystem Model for Understanding Regional Oceanography (NEMURO)”. The  
153 detailed configuration of the original NEMURO model, which represented pelagic plankton  
154 species (i.e., diatom, flagellate, and copepod), was described in Kishi et al. (2007). To address  
155 seasonality and interannual variability in ice algal production and biomass, a sea ice ecosystem  
156 was incorporated in the present work, (Fig. 2 and Table 1). In the developed model (called  
157 “Arctic NEMURO”, hereafter), the habitat of ice algae is confined to the 2-cm skeletal layer.  
158 The biogeochemical variables in the sea ice component comprise ice algae (IA), ice-related  
159 fauna (IF), nitrate (NO<sub>3</sub>), ammonium (NH<sub>4</sub>), silicate (SIL), dissolved organic nitrogen (DON),  
160 particulate organic nitrogen (PON), and opal (OPL). Each model grid has a single value per

161 variable independent of the ice thickness category. As the sea ice bottom temperature is always  
 162 kept at the freezing point of underlying seawater, a relationship of  $Q_{10} = 2$  adopted in the  
 163 present model did not have substantial impacts on biogeochemical cycles in the sea ice column.  
 164 The growth rate of ice algae (GR) is calculated depending on light condition (L) and nutrient  
 165 uptake ( $N_{up}$ ) terms:

$$166 \quad GR = GR_{max} \times L \times N_{up},$$

167 where the maximum growth rate  $GR_{max}$  is fixed at a constant value of  $0.8 \text{ d}^{-1}$ .

168 The light condition term followed the original NEMURO formulation:

$$169 \quad L = I / I_{opti} \times \exp(1 - I / I_{opti}),$$

$$170 \quad I = PAR_{frac} \times SW^{\downarrow} \times (1 - \alpha_{sfc}) \times \exp(-k_{snow} H_{snow} - k_{ice} H_{ice}),$$

171 where I is photosynthetically active radiation (PAR) in the skeletal layer. The conversion  
 172 coefficient from shortwave radiation to PAR ( $PAR_{frac}$ ) is 0.43 following the previous models  
 173 (Zhang et al., 2010; Dupont, 2012) so that 43% of shortwave flux is available for  
 174 photosynthesis activity. Light transmission through the snow and sea ice columns is given by  
 175 downward shortwave radiation from atmosphere ( $SW^{\downarrow}$ ), snow/ice surface albedo ( $\alpha_{sfc}$ ), column  
 176 thickness ( $H_{snow}$ ,  $H_{ice}$ ), and empirical extinction rates ( $k_{snow}$ ,  $k_{ice}$ ). The surface albedo ( $\alpha_{sfc}$ )  
 177 changes from 0.8 to 0.6 depending on snow/ice type and surface temperature during summer.  
 178 The light extinction rate ( $k_{snow}$ ,  $k_{ice}$ ) is set to  $0.12 \text{ cm}^{-1}$  for snow and  $0.045 \text{ cm}^{-1}$  for sea ice based  
 179 on Aota and Ishikawa (1982). According to this constant rate, for example, the light intensity in  
 180 the skeletal layer corresponds to approximately 10% (1%) of that absorbed into the surface of  
 181 sea ice with its thickness of 50 cm (100 cm) (Fig. 3a). The light transmission is calculated in  
 182 each thickness category (see the category arrangement in Section 2.1), and the under-ice  
 183 average intensity is then obtained in each model grid. A self-shading effect of ice algae is

184 neglected. For weak-light adaptation of ice algae, the optimal light intensity ( $I_{\text{opti}}$ ) is set to 10 W  
185  $\text{m}^{-2}$  (cf., 104  $\text{W m}^{-2}$  for pelagic phytoplankton (Kishi et al., 2007)). A PAR of 5 and 20  $\text{W m}^{-2}$   
186 results in a light condition term of 0.82 and 0.73, respectively (Fig. 3b).

187 The vertical exchange of biogeochemical variables between the skeletal layer and the ocean  
188 surface layer (suffixed as SKL and OCN, respectively, hereafter) is formulated in a different  
189 manner for sea ice freezing and melting periods. During the freezing period, ocean-to-ice fluxes  
190  $F_{\text{OI}}$  are proportional to sea ice freezing rate IFR:

$$191 \quad F_{\text{OI}} = CF_{\text{OI}} \times (\text{NO}_3, \text{NH}_4, \text{SIL}, \text{DON})_{\text{OCN}} \times \text{IFR}.$$

192 The proportional coefficient  $CF_{\text{OI}}$  is set to 0.3, since first-year ice salinity is able to reach  
193 approximately 30% of ocean salinity. In addition, all of the imported nutrients are accumulated  
194 only in the skeletal layer. The actual ice algae respond to nutrients concentrated in brine pockets  
195 and channels. However, the incorporation of such detailed structures in sea ice interiors is  
196 generally difficult for three-dimensional climate models. Here, we regard the skeletal layer as  
197 the reservoir of total imported nutrients under an idealized assumption. There is no import of  
198 particles such as pelagic planktons, PON, and OPL. During the melting period, ice-to-ocean  
199 fluxes  $F_{\text{IO}}$  are proportional to the sea ice melting rate IMR:

$$200 \quad F_{\text{IO}} = (\text{IA}, \text{IF}, \text{NO}_3, \text{NH}_4, \text{SIL}, \text{DON}, \text{PON}, \text{OPL})_{\text{SKL}} \times \text{IMR}.$$

201 According to this formulation, the concentration of all biogeochemical variables in the sea ice  
202 component decreases to zero when sea ice entirely disappears due to the melting process in  
203 each model grid. Although sea ice melts from its surface, bottom, and flank, respectively, it is  
204 difficult to separate these melting processes in terms of particle export. In general, ice surface  
205 meltwater sinks through internal brine channels and flushes out a part of materials in the  
206 skeletal layer (Vancoppenolle et al., 2010). Besides, ice algae have an ability to maintain their

207 position under a slow melting rate, and the habitat is not immediately lost even after ice bottom  
 208 melting. The methods adopted in the present work idealize ice-ocean exchange of  
 209 biogeochemical variables within reasonable scopes.

210 The nutrient source of ice algal growth can be divided between the sea ice column and  
 211 underlying seawater. The present study assumes that ice algae utilize both ice/ocean nutrients  
 212 depending on their biomass:

$$213 \quad N_{\text{up}} = RN_{\text{upSKL}} \times N_{\text{upSKL}} + (1 - RN_{\text{upSKL}}) \times N_{\text{upOCN}},$$

$$214 \quad RN_{\text{upSKL}} = 0.5 \times \{ \cos(\pi \times IA / KN_{\text{upSKL}}) + 1 \}, \text{ for } IA \leq KN_{\text{upSKL}},$$

215 where  $RN_{\text{upSKL}}$  is the ice algal uptake ratio of nutrient in the skeletal layer, and  $KN_{\text{upSKL}}$  is a  
 216 threshold value (Fig. 3c). When ice algal biomass  $IA$  exceeds  $KN_{\text{upSKL}}$ , only seawater nutrients  
 217 are utilized for the growth. The value of  $KN_{\text{upSKL}}$  is set to 1 mmol N m<sup>-2</sup> in the present  
 218 experiments. As reported in Section 3.2, sea ice nutrients are consumed preferentially for the  
 219 initial bloom of small-sized ice algae in early summer. According to the growth of ice algae,  
 220 their nutrient source shifts to seawater for the mature period. The “hybrid-type” formulation of  
 221 nutrient uptake represents more realistic ice algal biology, where ice algae anchoring under ice  
 222 floes gradually raise meter-long filaments in the water column (Boetius et al., 2013). In each  
 223 model time step, the Michaelis-Menten relationship is applied to nutrient concentration in the  
 224 skeletal layer and in the ocean surface layer (i.e., the uppermost ocean grid), respectively (Fig.  
 225 3d):

$$226 \quad N_{\text{upSKL}} = \min \{ \text{NO3}_{\text{SKL}} / (\text{NO3}_{\text{SKL}} + K_{\text{NO3}}) \times \exp(-\Psi_{\text{NH4}} \times \text{NH4}_{\text{SKL}}) \\$$

$$227 \quad \quad \quad + \text{NH4}_{\text{SKL}} / (\text{NH4}_{\text{SKL}} + K_{\text{NH4}}), \text{SIL}_{\text{SKL}} / (\text{SIL}_{\text{SKL}} + K_{\text{SIL}}) \},$$

$$228 \quad N_{\text{upOCN}} = \min \{ \text{NO3}_{\text{OCN}} / (\text{NO3}_{\text{OCN}} + K_{\text{NO3}}) \times \exp(-\Psi_{\text{NH4}} \times \text{NH4}_{\text{OCN}}) \\$$

$$229 \quad \quad \quad + \text{NH4}_{\text{OCN}} / (\text{NH4}_{\text{OCN}} + K_{\text{NH4}}), \text{SIL}_{\text{OCN}} / (\text{SIL}_{\text{OCN}} + K_{\text{SIL}}) \},$$

230 where the constant coefficients of half saturation for nitrate ( $K_{NO_3}$ ), ammonium ( $K_{NH_4}$ ), and  
231 silicate ( $K_{SIL}$ ) and of ammonium inhibition ( $\Psi_{NH_4}$ ) have the same values (Table 1) as those of  
232 pelagic diatoms (i.e., large phytoplankton PL in the NEMURO model) (Kishi et al., 2007).

233 The ice algal biomass decreases due to mortality, grazing, and sea ice melting. The  
234 respiration and mortality terms are functions of the ice algal biomass itself (under the freezing  
235 temperature assumption). In the present experiments, there is no biomass of ice-related fauna,  
236 and the grazing pressure on ice algae is neglected except for a sensitivity experiment in Section  
237 5.4. All ice algae are included in ice-derived PON without any biological activities after their  
238 export into the water column by melting sea ice. Sea ice assemblages sink faster than other  
239 particles derived from pelagic plankton because ice algae aggregate before the release from the  
240 sea ice bottom. Boetius et al. (2013) indicated rapid sinking of ice-related species. Hence, the  
241 modeled PON is divided into two components with different sinking speeds. The sinking speeds  
242 of PON derived from ice algae (pelagic plankton) are from 50–200  $m\ d^{-1}$  (2–200  $m\ d^{-1}$ ),  
243 following a cosine curve (Fig. 3e). The sinking speed is maintained at 200  $m\ d^{-1}$  below a depth  
244 of 1,000 m. These profiles are reasonable, because sinking of particulate organic materials  
245 generally accelerates with depth due to particle densification processes (e.g., aggregation in  
246 shallow depths and elimination of light/fragile organic materials at middle depths) (Honda et al.,  
247 2013). The modeled OPL is treated in the same manner. We refer to the fast- and slow-sinking  
248 PON/OPL as fPON/fOPL and sPON/sOPL, respectively.

249 The horizontal advection of biogeochemical variables in the sea ice component is also  
250 calculated, as the Arctic NEMURO is implemented in a three-dimensional framework. The  
251 divergence (convergence) of sea ice velocity causes loss (accumulation) of each material as  
252 well as snow and ice volumes. The actual ridging process is accompanied by complex

253 deformation, whereas the modeled sea ice ecosystem is kept consistently in the skeletal layer  
254 with a constant 2-cm thickness for simplicity.

255

### 256 **2.3 Experimental design**

257 The model domain contains the entire Arctic Ocean, the Greenland-Iceland-Norwegian Seas,  
258 and the northern part of the North Atlantic (Fig. 1). The horizontal resolution is 5 km, and there  
259 are  $1,400 \times 1,000$  grid points. There are 42 hybrid  $\sigma$ -z vertical levels. Vertical resolution varies  
260 from 2 m at the top to 500 m at the bottom. The  $\sigma$ -coordinate composed of three levels is  
261 applied to the uppermost 10 m. We performed two one-year experiments (called the 2011 and  
262 2012 cases), in which the 5-km grid model was integrated from October 2010 (2011) to  
263 September 2011 (2012) to examine seasonal and interannual variability in ice algae. The initial  
264 sea ice and ocean physical fields for these experiments were obtained from a 1979–2011  
265 decadal experiment using the 25-km grid version (Onodera et al., 2015). The atmospheric  
266 forcing components were constructed from the National Centers for Environmental  
267 Prediction/Climate Forecast System Reanalysis (NCEP/CFSR) 6-hourly dataset (Saha et al.,  
268 2010). Pacific water inflow is provided at the Bering Strait, based on Woodgate et al. (2005).  
269 Following our previous modeling study (e.g., Watanabe, 2011), the idealized seasonal cycles of  
270 northward velocity, temperature, and salinity are prescribed such that the annual mean inflow is  
271  $0.8 \text{ Sv}$  ( $1 \text{ Sv} \equiv 10^6 \text{ m}^3 \text{ s}^{-1}$ ) and temperature (salinity) reaches a maximum in September (March).  
272 Monthly nitrate and silicate concentrations derived from the World Ocean Atlas 2013 (Garcia et  
273 al., 2013) are used for a restoring along the lateral boundary region of the model domain, and  
274 summer climatology is assigned for the initial fields of ocean nutrients. As PON and opal in sea  
275 bottom sediments are crucial nutrient sources for the Arctic shelves via decomposition and

276 remineralization processes, the fluxes in ammonium, DON, and silicate are added to the deepest  
277 layers just above the shelf bottom as in Watanabe et al. (2014). Sea ice nutrients are initially  
278 non-existent in the skeletal layer, and the lowest ice algal concentration of  $0.02 \text{ mmol N m}^{-3}$  is  
279 given for initial growth (i.e., seeding). The relationship of  $1 \text{ mmol N} = 80 \text{ mgC} = 1.6 \text{ mgChl}$  is  
280 assumed using a C/Chl mass ratio of 50 and a C/N Redfield ratio of 6.625 to compare the model  
281 outputs with observational estimates, as in Watanabe et al. (2012). The detailed designs for  
282 sensitivity experiments are described in Section 5.

283

#### 284 **2.4 Sediment trap analysis**

285 The bottom-tethered sediment traps (SMD26S-6000, NiGK Cooperation) have been  
286 moored at Station NAP ( $75^\circ\text{N}$ ,  $162^\circ\text{W}$ , 1,975-m water depth) since October 2010. Deployment  
287 and turnaround were conducted by the Japanese R/V Mirai and the Canadian Coast Guard Ship  
288 Sir Wilfrid Laurier. Sinking particles were sampled at depths of 181–218 m (median, 184 m)  
289 during the first year from October 4, 2010 to September 27, 2011. The trap depth was 247–319  
290 m (median, 256 m) during the second year from October 4, 2011 to September 17, 2012. These  
291 sediment traps collected 26 samples approximately every two weeks during their one-year  
292 deployment. The recovered trap samples were sieved through 1-mm mesh to remove swimmers,  
293 and particles  $< 1 \text{ mm}$  were divided evenly into 10 sub-samples. One of 10 aliquot samples was  
294 filtered, and was desalted using Milli-W water. The dried sample was weighed, and it was then  
295 ground and mixed using an agate mill. PON and POC contents were analyzed in one sequence.  
296 The powdered samples were decalcified in hydrochloric acid vapor in a desiccator for eight  
297 hours to remove particulate inorganic carbon. Sodium hydroxide pellets were placed in the  
298 desiccator to neutralize the samples. PON content in the treated samples was sequentially  
299 analyzed by a CHN analyzer (NCS2500, Thermo Quest). Sinking PON flux was calculated

300 based on PON content, sampling period, open area of the sediment trap (0.5 m<sup>2</sup>), and aliquot  
301 size of the treated sample (1/10). The detailed analysis method and diatom valve fluxes were  
302 described in Onodera et al. (2015). The structures of radiolarians and copepods captured in the  
303 same traps were reported in Ikenoue et al. (2015) and Matsuno et al. (2015), respectively.  
304



### 305 **3. Seasonal transition in the Chukchi Borderland**

#### 306 **3.1 Physical environments**

307 We defined the NAP region as that enclosed by 74°–76°N and 159°–165°W for the  
308 following analyses (Fig. 1). Monthly mean values of the NCEP/CFSR cloud fraction,  
309 downward shortwave radiation, wind speed at a height of 10 m, snow depth, sea ice thickness,  
310 and sea ice concentration averaged in the NAP region are summarized in Table 2. The modeled  
311 physical variables were evaluated (Fig. 4). The NAP region was entirely covered by sea ice  
312 during the winter and spring seasons from December to April, and sea ice concentration  
313 decreased gradually from May to September in both the 2011 and 2012 cases (Fig. 4a). The  
314 area-mean sea ice thickness reached approximately 200 cm in April (Fig. 4b), which is a typical  
315 value north of the Chukchi Sea (Haas et al., 2010). The declines in sea ice concentration and  
316 thickness were consistent with the sea ice melting period from May to September (Fig. 4c). The  
317 mechanical divergence of sea ice flow fluctuated within the range of  $\pm 0.2 \text{ d}^{-1}$  in early winter  
318 and late summer (Fig. 4d).

319 Compared with the sea ice conditions simulated in the 2011 case, the early-winter covering  
320 of sea ice was somewhat delayed in the 2012 case. Although sea ice continued to melt until  
321 mid-November, winter sea ice thickness was greater in the 2012 case. The anomalous wind  
322 pattern could account for thicker ice transport toward the NAP region, as suggested in Section  
323 4.1. The negative anomaly of sea ice thickness in the 2011 case was additionally caused by two  
324 melting events in November and December (Fig. 4c) and the blanket effect of more snow  
325 accumulation on top of the sea ice (not shown). The faster rate of sea ice decline caused earlier  
326 sea ice opening in the 2012 case (Figs. 4a-b), partly due to lower surface albedo from less snow  
327 cover. These snow and sea ice differences were compatible with the NCEP/CFSR data (Table 2).

328 In addition, the enhanced mechanical divergence of sea ice flow from mid-July to August  
329 accelerated the sea ice reduction in 2012 (Fig. 4d). Ice algal biomass in a specific region can  
330 change based on sea ice divergence events. The detailed processes associated with cyclone  
331 activities are discussed in Section 4.4.

332 As ice algal primary production depends highly on nutrient conditions in the underlying  
333 ocean surface layer, replenishment of nitrate and silicate from depths in the nutricline is  
334 substantially important. The Ekman upwelling and downwelling velocities were calculated  
335 from the modeled ocean surface stress fields (i.e., the combination of wind stress in open water  
336 area and ice-ocean stress under sea ice). The week-long Ekman downwelling occurred in both  
337 cases during the winter, as usually seen inside the Beaufort Sea (Yang, 2009), and a strong  
338 upwelling event appeared in the 2011 case (Fig. 4e). In July–August, the Ekman velocity sign  
339 was opposite between the two cases. The mid-summer Ekman downwelling (upwelling) played  
340 a role in the nutricline deepening (shoaling) in the 2011 (2012) case. The vertical turbulent  
341 mixing was characterized by vertical diffusivity diagnosed using the closure scheme of Noh and  
342 Kim (1999) in the present model. Turbulent mixing was activated during winter in the 2011  
343 case (Fig. 4f). During the other periods, the smaller values of modeled vertical diffusivity by  
344 one or two orders indicated that the mixing process had a relatively minor impact on nutrient  
345 entrainment in the NAP region.

346

### 347 **3.2 Ice algal production**

348 The modeled ice algal production demonstrated remarkable spatial and interannual  
349 variability in the western Arctic Ocean (Fig. 5). Annual production exceeded  $0.6 \text{ mmol N m}^{-2}$   
350 over most of the Chukchi Sea shelf, whereas low productivity  $< 0.1 \text{ mmol N m}^{-2}$  was located in  
351 the central Canada Basin. The shelf-basin contrast in ice algal production was previously  
352 detected by the trans-Arctic Ocean expedition in the 1990s (Gosselin et al., 1997) and  
353 represented by decadal model simulations (Jin et al., 2012; Dupont, 2012). In the 2011 case, the  
354 local maximum appeared north of the Chukchi and Beaufort shelf breaks (Fig. 5a), whereas ice  
355 algal productivity was suppressed considerably around the Beaufort Gyre region in the 2012  
356 case (Fig. 5b). The negative anomaly widely covered the western Arctic except the coastal  
357 shelves and the northern part of Chukchi Borderland (Fig. 5c). Station NAP was located near  
358 the shelf-basin boundary and also showed the negative anomaly.

359 In the NAP region, the modeled ice algal bloom started in June and produced a peak  
360 biomass of  $0.7 \text{ mmol N m}^{-2}$  at the beginning of August in the 2011 case (Fig. 6a). The peak  
361 timing was a few months later than the pan-Arctic averages simulated in previous models (Jin  
362 et al., 2012; Deal et al., 2011), partly because the NAP region is located north of highly  
363 productive shelves. An additional reason for the lagged peak phase may be attributed to a lower  
364 photosynthetic response to incoming solar irradiance in the present model setting. Sensitivity to  
365 optimum light intensity is shown in Section 5.1. The Hovmöller diagram visualized the vivid  
366 shelf-basin contrast along the  $75^\circ\text{N}$  line (Fig. 6b). The bloom signal was quite weak inside the  
367 Canada Basin. A massive ice algal bloom up to  $10 \text{ mmol N m}^{-2}$  was simulated in July over the  
368 Chukchi northern shelf to the west of the NAP region. The modeled ice algal biomass north of  
369 the Chukchi Sea was within the lower range of  $1\text{--}340 \text{ mgChl m}^{-2}$  in Arctic sea ice (Arrigo et al.,

370 2010) and an order of magnitude smaller than that measured in Resolute Passage (160 mgChl  
371  $\text{m}^{-2}$ ; Michel et al., 1996). The Chukchi Borderland has shifted from a perennial ice-covered area  
372 to a seasonal ice zone in recent years. Multi-year ice would have dimmed the ice algal bloom in  
373 the past decades in this area. It is also reasonable that substantially lower amounts of nutrients  
374 restricted ice algal growth to the level below the pan-Arctic averages. In the 2012 case, initial  
375 bloom timing was further delayed by one month and ice algal biomass was clearly smaller than  
376 that of the 2011 case (Figs. 6a, c).

377 As introduced in Section 2.2, ice algal production rate was calculated using the empirical  
378 functions of light condition and nutrient uptake terms. The light condition in the skeletal layer  
379 of the sea ice column was recovered slowly after the end of polar night (February in the NAP  
380 region) and then increased rapidly due to thinning of snow/ice in May (Fig. 7a). Peak values of  
381 PAR ( $3.5 \text{ W m}^{-2}$  in the 2011 case, and  $2.2 \text{ W m}^{-2}$  in the 2012 case) were recorded in mid-July  
382 after the summer solstice. Although sea ice melting continued until September, light intensity  
383 turned to decrease in accordance with the annual cycle of solar radiation. As the optimal light  
384 intensity for ice algal growth ( $I_{\text{opti}}$ ) was set to  $10 \text{ W m}^{-2}$  in the present experiments, the light  
385 condition term varied in phase with the PAR transition (Fig. 7b). The weaker summer light  
386 intensity in the 2012 case could be attributed to the depressed shortwave radiation due to more  
387 cloud cover (Table 2), despite thinner sea ice in August (Fig. 4b). The cyclone impact on light  
388 conditions is described in Section 4.4.

389 The nutrient conditions in the sea ice and water columns showed remarkable interannual  
390 variability. Sea ice nitrate content peaked at  $0.6 \text{ mmol N m}^{-2}$  ( $0.2 \text{ mmol N m}^{-2}$ ) in the 2011  
391 (2012) case (Fig. 8a), which was an order of magnitude smaller than in landfast ice in Resolute  
392 Passage of the Canadian Archipelago (Cota and Smith, 1991). Potential factors contributing to

393 the difference include the nutrient environment in the underlying water column and the sea ice  
394 freezing rate, because nutrient accumulation in the skeletal layer was induced by ocean-to-ice  
395 flux during the sea ice freezing period (see formulation in Section 2.2). At the beginning period  
396 of the one-year model integration, the nutricline depth was located at 20 m in the NAP region  
397 (Figs. 8b-c). Ekman downwelling helped deepen the nutricline from October to early November  
398 in both cases (Fig. 4e). In the 2011 case, Ekman upwelling was also evident in November.  
399 However, the duration was just one week, so the Ekman contribution with a peak of  $0.8 \text{ m d}^{-1}$   
400 played a minor role in nutrient entrainment. The more important contributory process was  
401 strong mixing during winter in the 2011 case, as shown by the enhanced vertical diffusivity (Fig.  
402 4f). According to these processes, the surface nitrate concentration reached  $2 \text{ mmol N m}^{-3}$  (Fig.  
403 8b), and a significant part was imported into the skeletal layer (Fig. 8a). In contrast, the  
404 oligotrophic water stayed over the nutricline, which was at a nearly constant depth or somewhat  
405 deepened during winter in the 2012 case (Fig. 8c). Sea ice nitrate content reflected the ocean  
406 surface value of  $< 1 \text{ mmol N m}^{-3}$ . Sea ice silicate, which had a similar difference to nitrate, was  
407 not a limiting factor for ice algal growth in the NAP region (not shown). The rate of sea ice  
408 freezing also differed between the two cases. The total amount of thermal sea ice growth from  
409 October to April was 160 (136) cm in the 2011 (2012) cases. Whereas we focused on the  
410 seasonal transitions from winter to early summer, *in-situ* data of nutrient concentration and sea  
411 ice freezing rate were unavailable for the target region and period. Accordingly, proper  
412 evaluations of the modeled properties, particularly during winter, were difficult at this stage. At  
413 least, the model results suggest that the nutrient accumulation in the skeletal layer during the  
414 freezing period controls the interannual variability in the initial ice algal bloom. The influences

415 of the basin-scale wind pattern and water mass transport on the nutrient environment are  
416 analyzed in Section 4.

417 Nutrient availability for ice algal production reflected the difference in this preconditioning.  
418 Based on the present model formulation, sea ice nutrients were consumed primarily during an  
419 initial stage of the ice algal bloom, and nutrients in the ocean surface layer were utilized for  
420 further blooms. According to ice algal growth (Fig. 6a), the uptake ratio of sea ice nutrients  
421 ( $RN_{upSKL}$ ) shifted from 1 to 0.7 within a few weeks of July in the 2011 case (Fig. 7c). When the  
422 half-saturation constant for nitrate uptake ( $K_{NO_3}$ ) was set to  $6 \text{ mmol N m}^{-3}$  for ice algae as well  
423 as pelagic diatoms (PL in the present model), the nitrate uptake term before the ice algal bloom  
424 was approximately 0.9 (0.7) in the 2011 (2012) case (Fig. 7d). The growth ratio between the  
425 two cases became 1.8 at the beginning of June after multiplying the light condition term (Fig.  
426 7b). The larger growth rate accounted for the earlier initial ice algal bloom in the 2011 case (Fig.  
427 6a). Sea ice nitrate was depleted rapidly by this initial bloom and partially by export to the  
428 water column with melting sea ice (Fig. 8a). The subsequent decrease in the  $RN_{upSKL}$  value  
429 represented utilization of the underlying seawater nutrients (Fig. 7c). The additional bloom  
430 occurred in late July (Fig. 6a). In the 2012 case, the decrease in the nutrient uptake term lagged  
431 behind the 2011 case in accordance with the delay of the initial bloom (Fig. 7d). The ocean  
432 nutrient uptake term, which had lower values during the ice freezing period, gradually became  
433 comparable with the 2011 case. However, the higher  $RN_{upSKL}$  value, except in early August,  
434 restricted ocean nutrient uptake in the 2012 case (Fig. 7c).

435 As expected, the seasonal transition of the ice algal biomass was similar to daily primary  
436 productivity (Figs. 9a-b). In the present model experiments, primary production derived from  
437 nutrients in the skeletal layer and in the water column was calculated separately. In the 2011

438 case, the nutrient source for the ice algal bloom changed from the sea ice column for the first  
439 primary production peak of  $23 \mu\text{mol N m}^{-2} \text{d}^{-1}$  to seawater for the second larger peak of  $82 \mu\text{mol}$   
440  $\text{N m}^{-2} \text{d}^{-1}$ . The second peak value of  $\sim 6.6 \text{ mgC m}^{-2} \text{d}^{-1}$  was close to the field-based estimates of  
441  $4\text{--}9 \text{ mgC m}^{-2} \text{d}^{-1}$  on the Beaufort shelf and slopes (Gradinger, 2009) and  $< 10 \text{ mgC m}^{-2} \text{d}^{-1}$  in  
442 the Arctic basins (Deal et al., 2011). The model results indicate that nutrients imported by sea  
443 ice freezing determine the beginning of the ice algal bloom, and that ocean nutrients have a  
444 greater contribution to annual ice algal production, as reported previously (Gradinger, 2009).  
445 The comparison with the PON export to the underlying water column suggested that more than  
446 half of the organic nitrogen was remineralized in the sea ice column (Fig. 9a). In the 2012 case,  
447 the peak of primary production simulated in early August was  $35 \mu\text{mol N m}^{-2} \text{d}^{-1}$  (Fig. 9b). The  
448 relative contribution of ocean nutrients to primary productivity was less than that in the 2011  
449 case. The August peak in PON export flux exceeding ice algal productivity was attributed to  
450 lateral advection of shelf-origin sea ice floes. Detailed discussions are presented in Section 4.3  
451 and 4.4.  
452

#### 453 **4. Wind-driven dynamics associated with ice algal productivity**

454 To examine background mechanisms for year-to-year changes in ice algal productivity,  
455 wind-driven sea ice and ocean dynamics in the western Arctic Ocean were addressed.

456

#### 457 **4.1 Wind and sea ice patterns**

458 Interannual variabilities in sea ice motion and ocean surface currents in the Beaufort Sea  
459 are closely related to the atmospheric circulation pattern (Yang, 2009; Proshutinsky et al., 2009).  
460 We compared the winter mean sea level pressure (SLP) and wind stress fields constructed from  
461 the NCEP/CFSR reanalysis data between the two years. Wind stress was calculated from the  
462 daily mean SLP using a protocol of the Arctic Ocean Model Intercomparison Project (AOMIP)  
463 (<http://www.whoi.edu/page.do?pid=30576>). An anti-cyclonic wind pattern was accompanied by  
464 a weak Beaufort High around the Canada Basin during winter 2010–2011 (Fig. 10a). The  
465 easterly wind in the southern Beaufort Sea was favorable for transporting Chukchi shelf water  
466 toward the southern Canada Basin and the NAP region via the Ekman process. Ekman transport  
467 was analytically estimated with a seawater density of  $1.025 \times 10^3 \text{ kg m}^{-3}$  and a Coriolis  
468 coefficient of  $1.4 \times 10^{-4} \text{ s}^{-1}$ . A sea ice-ocean stress value of 0.1 Pa, which was frequently  
469 recorded along the Chukchi shelf break during early winter in the 2011 case, yielded an Ekman  
470 transport value of  $0.7 \text{ m}^2 \text{ s}^{-1}$  ( $1.8 \text{ km}^2 \text{ mon}^{-1}$ ). This value is close to the November climatology  
471 in the southern Beaufort Sea (Yang, 2009) and indicates a shelf-basin water exchange of 900  
472  $\text{km}^3 \text{ mon}^{-1}$  for a shelf break axis length of 500 km. In contrast, high SLP extended from the  
473 Siberian Arctic to the western Arctic Ocean in winter 2011–2012 (Fig. 10b). Accordingly, a  
474 northwesterly wind prevailed in the Beaufort Sea. In this situation, no definite shelf water  
475 transport toward the NAP region was expected by the winter wind fields.



476 The changes in wind patterns were consistent with the modeled physical environments in  
477 the NAP region, where several differences between the 2011 and 2012 cases were described in  
478 Section 3.1. For October to early November 2011 (i.e., the beginning period of the 2012 case),  
479 localized anti-cyclonic wind forcing was closely related to the modeled negative rate of sea ice  
480 growth, convergence of sea ice velocity, and Ekman downwelling in the NAP region (Figs. 4c-  
481 e). The wind-driven warm water intrusion toward the marginal ice zone induced lateral/bottom  
482 melting of sea ice floes (not shown). Sea ice convergence increased sea ice thickness via  
483 mechanical ridging processes, in contrast to sea ice melting occurring during the same period.  
484 Continuous Ekman downwelling coincided with the sea ice convergence. For the period  
485 afterwards, the positive anomaly of sea ice thickness was produced by southward transport of  
486 thicker sea ice from the central Arctic in the 2012 case (Fig. 4b). The direction of sea ice flow  
487 around the NAP region clearly differed between the two years (Figs. 10c-f), as detected  
488 previously by satellite-based and modeled spatial patterns (Onodera et al., 2015). Both the daily  
489 time series in the Polar Pathfinder sea ice motion vectors (Fowler et al., 2013) and in the  
490 simulation results showed the successive southward advection of sea ice from late October 2011  
491 to January 2012 (Figs. 10d, f). Sea ice moved several hundred km during this period when sea  
492 ice velocity was  $5 \text{ cm s}^{-1}$  (ca.  $130 \text{ km mon}^{-1}$ ). These results suggest that the anomalous wind  
493 pattern forced southward transport of oligotrophic sea ice and water masses within the Beaufort  
494 Gyre and eventually reduced nutrient availability in the Chukchi Borderland.

495

#### 496 **4.2 Nutrient and shelf-break tracer distributions**

497 The nutrient preconditioning that occurred before the ice algal blooming period reflected  
498 the wind-driven sea ice and water mass transport, as suggested in Section 4.1. The spatial  
499 distribution of the ocean nitrate concentration was characterized by a sharp meridional gradient

500 across the Chukchi and Beaufort shelf breaks (Figs. 11a-b), as captured by a number of ship-  
501 based observations (e.g., Nishino et al., 2011). The modeled vertical average in the top 30 m  
502 reached  $10 \text{ mmol N m}^{-3}$  in the central Chukchi Sea and was  $< 1 \text{ mmol N m}^{-3}$  in the Canada  
503 Basin. As shown in Fig. 8, nitrate content around the NAP region tended to differ. In the 2011  
504 case, relatively high nitrate concentrations were distributed from the northern shelf of the  
505 Chukchi Sea to east of Northwind Ridge along  $75^\circ\text{N}$  (Fig. 11a). On the other hand, the shelf-  
506 basin contrast in nitrate content was still apparent even in the southern area of Chukchi  
507 Borderland in the 2012 case (Fig. 11b).

508 To explore the paths of the shelf-break water, a virtual passive tracer was provided along  
509 the shelf-basin boundary. We chose the tracer source region sandwiched between the 100–200-  
510 m isobaths. The tracer value was fixed at 1.0 (i.e., 100% concentration) for depths of 0–200 m  
511 in the defined region through each one-year experiment. Advection and diffusion of the tracer in  
512 the other regions were calculated as well as seawater temperature and salinity. The modeled  
513 distribution in March 2011 indicated that the tracer provided along the shelf-basin boundary  
514 region was transported from the Chukchi northern shelf toward the interior of the Canada Basin.  
515 The northern edge of the tracer matched the nitrate-rich area in the 2011 case (Fig. 11a). The  
516 vertical profile of nitrate concentration in the NAP region reflected the deepening nutricline  
517 driven by the Ekman downwelling in October (Figs. 4e and 11c). Subsequently, nitrate content  
518 in the upper 50 m showed a net increase during December–January, which could be explained  
519 by lateral input rather than local vertical mixing. Hence, the model results indicate that Ekman  
520 transport of Chukchi shelf water along with energetic turbulent mixing enhanced nutrient  
521 availability for ice algae in the NAP region. In contrast, in March 2012, the tracer signal was  
522 quite weak over the Chukchi Borderland (Fig. 11b). No significant change occurred in the

523 vertical nitrate profile during winter after the wind-driven downward shift (Fig. 11d). The  
524 spread of fresher basin water blocked the intrusion of shelf water and weakened the turbulent  
525 mixing. The density stratification plausibly controlled ocean subsurface mixing, as wind speed  
526 averaged from November to January of the 2011 and 2012 winter periods was comparable  
527 (Table 2). This mechanism was consistent with previous findings, in which the mixed layer  
528 depth correlated with hydrographic structures rather than wind forcing in the western Arctic  
529 (Peralta-Ferriz et al., 2015).

530 Onodera et al. (2015) categorized the sinking diatom assemblages in the sediment trap  
531 samples at Station NAP into 98 taxa. The dominant species during summer 2011 were *Fossula*  
532 *arctica* and the *Fragilariopsis* group (*F. cylindrus* and *F. oceanica*), which are common in ice  
533 algae in the shelf region (Cremer, 1999). Their relative abundances were minor in the sinking  
534 diatom flora during summer 2012. Instead, the major diatoms in August 2012 were planktonic  
535 species such as *Thalassionema nitzschioides*, which was commonly observed in the Canada  
536 Basin. In addition, the sinking flux of total diatom valves in August 2012 was considerably  
537 lower than that in August 2011. The observed diatom compositions and valve fluxes were  
538 consistent with the above-mentioned physical backgrounds. The modeled nitrate distribution  
539 and tracer pathway supported the suggestion that winter transport of oligotrophic water from  
540 the interior of the Canada Basin toward the NAP region was an important factor suppressing ice  
541 algal productivity during summer 2012.

542

#### 543 **4.3 PON flux**

544 The time series of sinking PON flux in the NAP region was compared with the sediment  
545 trap data. The modeled PON flux at 180 m in the 2011 case increased gradually from June and  
546 peaked at  $18 \mu\text{mol N m}^{-2} \text{d}^{-1}$  in mid-August following the ice algal bloom (Fig. 9c). Flux > 8

547  $\mu\text{mol N m}^{-2} \text{d}^{-1}$  continued until the end of the model integration (i.e., September). The flux  
548 amount was underestimated in August and became comparable afterward with the trap values.  
549 The PON flux at 180 m corresponded to 79% of the ocean surface value exported from the sea  
550 ice bottom during July–September 2011 (Figs. 9a, c). It should be noted that ice algae released  
551 from the skeletal layer were included immediately in the ice-derived PON without their  
552 biological activities in the present model setting. The major component of the PON flux  
553 originated from ice algae, as observed in the analysis of diatom valve compositions (Onodera et  
554 al., 2015). The PON flux derived from pelagic phytoplankton and zooplankton increased  
555 gradually in August and peaked at  $6 \mu\text{mol N m}^{-2} \text{d}^{-1}$  in early September (Fig. 9c). In the 2011  
556 case, the dominance of the ice-derived PON for the sinking flux was associated with a faster  
557 sinking speed (Section 2.2 and Fig. 3e), although the total biomass of pelagic plankton groups  
558 was an order of magnitude larger than that of the ice algal biomass (not shown). The sediment  
559 trap data captured another peak in PON flux during May 2011, when the model experiment  
560 could not reproduce the peak. The thick ice cover restricted spring bloom of ice algae and  
561 pelagic phytoplankton in the NAP region (Fig. 4b and Table 2). Instead, this event may have  
562 been caused by transport of shelf water with lithogenic materials of sea bottom sediment. A  
563 candidate driver was a cold-core eddy generated from a narrow jet along the Chukchi shelf  
564 break (Spall et al., 2008; Llinás et al., 2009). The background mechanisms for the spring peak  
565 are beyond the scope in the present study and will be analyzed in the future.

566 PON flux in the 2012 case produced a distinct mid-summer peak at the ocean surface and  
567 at 180 m, although the trapped sample volume was too low to estimate nitrogen content in  
568 summer 2012 (Fig. 9b, d). The trap depth of 247–319 m in 2012, which was deeper than that of  
569 181–218 m in 2011, may have caused biases in the comparison between the two years.

570 Importantly, PON flux in 2012 was markedly lower than the 1,300-m flux in 2011 (Onodera et  
571 al., 2015). Again, most of the modeled PON flux was ice-derived. The contribution of pelagic-  
572 derived PON in the 2012 case was less than in the 2011 case. Enhanced sea ice melting of up to  
573  $4 \text{ cm d}^{-1}$  assisted the peak flux in early August (Fig. 4c). The ice-ocean flux was remarkably  
574 greater than the ice algal production rate, indicating that one-dimensional sea ice processes  
575 cannot account for PON flux in the NAP region (Figs. 9b). We trace lateral advection of the ice  
576 algal biomass around the Chukchi Borderland in the next section.

577

#### 578 **4.4 Impact of great cyclone activity**

579 It was suggested that an extreme cyclone event was a supplementary factor for the drastic  
580 sea ice reduction, particularly in the western Arctic, and the subsequent record minimum extent  
581 of Arctic sea ice in summer 2012 (Simmonds and Rudeva, 2012; Zhang et al., 2013). A  
582 previous modeling analysis indicated that plankton productivity over the Chukchi, East Siberian,  
583 and Laptev shelves was enhanced by vertical mixing with nutrient replenishment and lateral  
584 plankton transport from the western Arctic basin during the cyclone storm (Zhang et al., 2014).  
585 It is assumed that synoptic cyclone activities have both positive and negative contributions to  
586 ice algal production. In the 2012 case, the event-like shoaling of the upper part of the nutricline  
587 was caused by mixing and upwelling processes in the NAP region, where the southern part of  
588 the great cyclone passed and marginal ice floes were located in early August (Fig. 12a). The  
589 modeled vertical diffusivity was maintained at background values partly because strong density  
590 stratification suppressed turbulent mixing until July 2012 (Fig. 4f). During the cyclone event  
591 with high wind speeds (Table 2), vertical mixing of nearly  $10 \text{ cm}^2 \text{ s}^{-1}$  reached a depth of 20 m  
592 (Figs. 4f). Besides, the Ekman upwelling that continued from July 15 to August 29 could have  
593 worked on nutricline shoaling of 3.3 m (Fig. 4e). However, this timing of nutrient

594 replenishment overlapped with the release of ice algae from the skeletal layer due to active sea  
595 ice melting (Fig. 8c), and the mixing and upwelling processes hardly enhanced ice algal  
596 productivity. Mechanical sea ice divergence associated with cyclonic wind fields rather  
597 contributed to the reduction in ice algal biomass in the specific region (Fig. 4d). Whereas the  
598 outward movement of sea ice floes itself did not lead to loss of ice algae, solar heat absorption  
599 into the exposed open water fractions enhanced lateral/bottom melting of sea ice and  
600 corresponding release of ice algae. The light conditions for ice algal growth also changed by  
601 during the cyclone event with extensive cloud cover. The NCEP/CFSR reanalysis data showed  
602 a depression in solar irradiance in the southern part of the cyclone passage, where an early  
603 August shortwave flux in 2012 was lower than that in 2011 by approximately  $20 \text{ W m}^{-2}$  (not  
604 shown). The negative anomaly of light intensity corresponded to a decrease in the light  
605 condition term for ice algal growth by less than 0.1 (Fig. 3b).

606       Here, we performed a sensitivity experiment in which all biogeochemical processes in the  
607 sea ice ecosystem were halted in August 2012. In this idealized experiment (called the “no ice  
608 algal activity case”), only lateral advection and sea ice-ocean fluxes were allowed in the sea ice  
609 column. All physical and pelagic marine ecosystem processes were calculated as in the original  
610 2012 case. Although there was no ice algal production locally in August, both the modeled ice  
611 algal biomass and PON flux increased in the NAP region (Figs. 12c-d). These enhanced signals  
612 could only be explained by horizontal transport of larger biomass from neighboring regions.  
613 The differences from the original case corresponded to additional production of ice algae  
614 flowing into the NAP region. Thus, lateral advection was essentially important during the 2012  
615 cyclone period.

616 In the 2012 case, westerly winds were intensified in the southern part of a cyclone passage  
617 and transported shelf-origin ice algal patches toward the Northwind Ridge. Each sea ice floe  
618 moved approximately 150 km eastward during August 3–10 (Fig. 12b). Although the direction  
619 of sea ice motion ( $87.4^\circ\text{T}$ ) was similar to the satellite-based vectors ( $82.8^\circ\text{T}$ ), the modeled drift  
620 speed ( $20.3 \text{ cm s}^{-1}$ ) was markedly faster than the latter ( $5.1 \text{ cm s}^{-1}$ ) during the cyclone period. It  
621 is plausible that the peculiar advection caused a sudden increase in ice algal biomass and an  
622 overestimation of the modeled PON flux in the NAP region (Figs. 6a and 12b). Local biases on  
623 sea ice velocity may have arisen from atmospheric momentum input and sea ice dynamics. In  
624 the present experiments, the conversion from SLP to the wind stress field (i.e., the AOMIP  
625 protocol referred to in Section 4.1) was formulated with specific turning angles, which varied  
626 depending on geostrophic wind speed (Proshutinsky and Johnson, 1997). Uncertainties in the  
627 reanalysis SLP data should also be considered, because the maximum strength of the great  
628 cyclone in August 2012 calculated from the data assimilation system depended on the number  
629 of radiosonde profiles (Yamazaki et al., 2015). In addition, the traditional rheology of sea ice  
630 internal stress has been developed for climate models with grid spacing much coarser than 10  
631 km and does not guarantee the accuracy of ice floe dynamics, especially in the marginal ice  
632 zone. Thus, speed and direction of the modeled ice algal advection around the Chukchi  
633 Borderland may have deviated in August 2012. These biases had less impact on the basin-scale  
634 sea ice and ocean circulation.

635 Another concern is the event-like deepening of the shallow sediment trap at Station NAP in  
636 July 2012 (Onodera et al., 2015). An intensified ocean current occasionally inclines the upper  
637 part of the bottom-tethered mooring system during storms. The anchored sea bottom depth of  
638 1,975 m and deepening of the trap from 260 to 320 m suggests an inclination angle of

639 approximately  $15^\circ$ . It was reported that trapping efficiency and particle components were  
640 remarkably influenced by tilting  $> 30^\circ$  (Gardner, 1985). If this previous examination can be  
641 applied despite the different trap shape, a  $15^\circ$  tilt should not significantly impact trapping  
642 efficiency. In addition, strong ocean currents  $> 10 \text{ cm s}^{-1}$  sometimes reduce trapping efficiency  
643 (Baker et al., 1988). However, the modeled horizontal velocity at the trap depths was below 2  
644  $\text{cm s}^{-1}$ , even during the cyclone period (not shown). It should also be noted that the trapped  
645 PON flux was continuously negligible throughout summer 2012, not only for the temporal  
646 cyclone event.

647



## 648 **5. Sensitivity experiments**

649 Although the present model experiments show the interannual variability in ice algal  
650 primary production and sinking biogenic particle flux in the NAP region, various sea ice-related  
651 processes still need to be considered. Here, we refer to the 2011 case analyzed in previous  
652 sections as the original case and performed sensitivity experiments using different model  
653 settings (Fig. 13 and Table 3). The first three cases (Cases 1–3) address uncertainties in the  
654 model parameters. In the next three cases (Cases 4–6), the grazing pressure on ice algae and the  
655 treatments of ice algae released into the water column are discussed. All the sensitivity  
656 experiments were initiated from the modeled fields at the beginning of March in the original  
657 case and conducted until September (i.e., seven months integration).

658

### 659 **5.1 Optimum light intensity for ice algal production (Case 1)**

660 It is difficult to estimate accurately the photosynthesis-irradiance relationships of ice-  
661 related flora. Ice algae adapt well to weaker light intensity compared with that of pelagic  
662 phytoplankton (Arrigo et al., 2010). In the original case, the optimum light intensity for ice  
663 algal production  $I_{\text{opti}}$  was set to  $10 \text{ W m}^{-2}$ . Gradinger (2009) reported that the minimum  
664 requirement for ice algal growth was typically  $< 1 \mu\text{E m}^{-2} \text{ s}^{-1}$  based on laboratory incubation  
665 experiments. When the relationship of  $1 \text{ W m}^{-2} \sim 4.56 \mu\text{E m}^{-2} \text{ s}^{-1}$  is applied following Lavoie et  
666 al. (2005),  $I_{\text{opti}}$  may be a smaller value. Here, we performed two sensitivity experiments with  
667 different  $I_{\text{opti}}$  values (Case 1). When  $I_{\text{opti}}$  was set to  $5 \text{ W m}^{-2}$  ( $20 \text{ W m}^{-2}$ ), the summer peak in the  
668 light condition term was 0.9 (0.3) in the NAP region (Figs. 3b and 7a). Relaxing the light  
669 limitation resulted in an earlier and stronger ice algal bloom (Fig. 14a). The initial bloom  
670 occurred in early June and the second peak of ice algal biomass increased to  $1.2 \text{ mmol N m}^{-2}$  (cf.

671 0.7 mmol N m<sup>-2</sup> in the original case). The phase and magnitude of the modeled PON flux  
672 shifted similarly and were still comparable with the trap data (Fig. 14b). In contrast, restricted  
673 light conditions dampened the ice algal productivity to a peak biomass of 0.1 mmol N m<sup>-2</sup> (Fig.  
674 14a). The resultant decreased release of ice algae into the water column delayed the seasonal  
675 increase in the PON flux (Fig. 14b). The difference in ice algal biomass did not alter the flux  
676 during late summer, which was derived mainly from pelagic plankton. Based on these  
677 sensitivity experiments, an optimum light intensity of 10 W m<sup>-2</sup> or below was recommended for  
678 the formulation adopted. Other choices can be made for the light condition term. Ice algae may  
679 not suffer from photo-inhibition even when the skeletal layer receives strong irradiance diffused  
680 from neighboring open leads during ice melting periods. A saturated light condition in  
681 accordance with increasing PAR can be represented, for example, by the hyperbolic tangent  
682 function used in Lavoie et al. (2005). Besides, the shelf-shading effect of ice algae reduces ice  
683 algal productivity in massive blooming regions (Pogson et al., 2011).

684

## 685 **5.2 Nutrient sources for ice algal production (Case 2)**

686 The present model adopted the hybrid nutrient uptake formulation. Ice algal productivity  
687 depends on the uptake ratio between sea ice and water nutrients. Here, we performed three  
688 experiments (Case 2). When the threshold value  $KN_{upSKL}$  is increased to 1.5 mmol N m<sup>-2</sup>, (cf.  
689 1.0 mmol N m<sup>-2</sup> in the original case), the ice algal growth rate reflects nutrient availability in  
690 the sea ice column more strongly (Fig. 3c). Conversely, the decrease in  $KN_{upSKL}$  to 0.5 mmol N  
691 m<sup>-2</sup> accelerates the uptake of seawater nutrients. However, the modeled ice algal biomass and  
692 PON flux were not sensitive to this range of  $KN_{upSKL}$  (Figs. 14c-d). As in the original case (Figs.  
693 7c and 9a), the major source of ice algal production was seawater nutrients, even when only

694 20% of the biomass could utilize (i.e.,  $RN_{upSKL} = 0.8$ ). On the other hand, both the ice algal  
695 biomass and PON flux dropped remarkably in another experiment, in which uptake of sea ice  
696 nutrients was halted throughout the integration period (Figs. 14c-d). The slower growth rate  
697 with lower concentrations of seawater nutrients prevented ice algal seeds from blooming to the  
698 same level as in the original case before sea ice melting loss (Fig. 7d). The nutrient reservoir  
699 (and high concentration) in the sea ice column is important for the initial acceleration in an ice  
700 algal bloom, and nutrient availability in the ocean surface layer controls peak biomass.

701 The exchange rate of dissolved materials at the ice-water interface generally depends on  
702 molecular and turbulent diffusion processes. Lavoie et al. (2005) assumed that nutrient  
703 replenishment from the underlying mixed layer was proportional to friction velocity varying  
704 with the tidal cycle. The tidal effect is important in some regions such as the narrow straits of  
705 the Canadian Archipelago. However, exchange processes other than tidal mixing would also be  
706 necessary for the pan-Arctic Ocean modeling. In this connection, the ocean-to-ice nutrient flux  
707 is proportional to the  $CF_{OI}$  coefficient during the ice freezing period. A  $CF_{OI}$  value of 0 or 1 is  
708 clearly unrealistic, because a significant portion of *in-situ* seawater nutrients remains inside the  
709 sea ice column, and the residual is ejected to the underlying water column after sea ice freezing  
710 as well as salinity. The original case adopted a  $CF_{OI}$  value of 0.3, following a first-year ice  
711 salinity of  $\sim 10$  psu. Smaller  $CF_{OI}$  values suppress nutrient accumulation in the skeletal layer  
712 during the freezing period and delay the initial ice algal bloom. Another assumption in the  
713 present model is that all of the sea ice nutrients are concentrated only in the skeletal layer with  
714 its constant thickness (cf. 2 cm in the original case), instead of brine pockets and channels that  
715 were not represented in the present model. An increase in the layer thickness reduces nutrient  
716 “concentration” (not total amount integrated in the entire sea ice column) and consequently

717 delays an ice algal bloom. For example, a nitrate content of  $0.6 \text{ mmol N m}^{-2}$ , which was  
718 recorded in April of the original 2011 case (Fig. 8a), yields a concentration of  $30 \text{ mmol N m}^{-3}$   
719 ( $12 \text{ mmol N m}^{-3}$ ) and a nitrate condition term of 0.91 (0.80) in the skeletal layer with 2-cm (5-  
720 cm) thickness. A time-varying biologically active layer with brine volumes (Tedesco et al.,  
721 2010) and multiple separate sea ice layers (Pogson et al., 2011) have been proposed to represent  
722 ice algal habitats more precisely. These uncertainties in sea ice nutrients seem to have an impact  
723 on ice algal production.

724

### 725 **5.3 Sinking speed of ice-derived PON (Case 3)**

726 The present model prescribed the fixed vertical profile of particle sinking speed (Fig. 3e).  
727 In the original case, the sinking speed of ice-derived PON varied from  $50 \text{ m d}^{-1}$  in the  
728 uppermost model layer to  $200 \text{ m d}^{-1}$  at a depth of 1,000 m. This speed range was comparable  
729 with the previous estimate of  $> 85 \text{ m d}^{-1}$  between the shallow (180 m) and deep (1,300 m) traps  
730 at Station NAP in August 2011 (Onodera et al., 2015). The PON exported from the sea ice  
731 bottom reached a depth of 180 m within four days under the model profile. As the  
732 decomposition rate from PON to ammonium and DON was set to  $0.2 \text{ d}^{-1}$  at  $0 \text{ }^\circ\text{C}$ , approximately  
733 half (47%) of the ice-derived PON was dissolved above a depth of 180 m. Here, we performed  
734 two experiments (Case 3), in which the minimum sinking speed was set to 200 (20)  $\text{m d}^{-1}$  in the  
735 faster (slower) sinking case (cf.  $50 \text{ m d}^{-1}$  in the original case). The remaining ratio of ice-  
736 derived PON after dissolution in these cases is theoretically 82% and 20% at a 180-m depth,  
737 respectively. Sinking speed hardly affected ice algal biomass (Fig. 14e), although the vertical  
738 nutrient profile in the water column had quite minor changes. On the other hand, PON flux  
739 differed significantly between the two cases (Fig. 14f). The earlier and larger peak in the PON

740 flux appeared in the faster sinking case. The flux range obtained in Case 3 was smaller than the  
741 sensitivity to the optimum light intensity evaluated in Case 1.

742 Actual sedimentation of biogenic particles depends on the ballast distribution in addition to  
743 aggregation and elimination of light/fragile organic materials. When the source region of sea ice  
744 and surface water in the NAP region was the central Canada Basin, an insufficient quantity of  
745 ballast particles would have allowed slower PON sinking (Honjo et al., 2010). A variable  
746 sinking speed depending ballast particles may improve a model performance on the PON flux.  
747 Besides, the PON derived from phytoplankton and zooplankton possibly has a different sinking  
748 speed. The faster sinking speed of fecal pellets may account for a substantial portion of the  
749 particle flux as observed in Resolute Passage (Michel et al., 1996). Thus, many uncertainties  
750 remain with respect to the PON sinking process.

751

#### 752 **5.4 Grazing on ice algae (Case 4)**

753 Previous observations detected a significant quantity of ice-related fauna including  
754 amphipods in the sea ice column (Bluhm et al., 2010). It was also reported that ice algal  
755 assemblages suspended under the ice bottom layer were an important food source for pelagic  
756 grazers (e.g., copepods) during the early stages of sea ice melting (Michel et al., 1996). Here,  
757 the impact of the grazing process on ice algal biomass was examined (Fig. 13). In Case 4, the  
758 concentration of ice-related fauna (IF) changed from zero in the original case (i.e., no grazing  
759 pressure on ice algae throughout the integration period) to 0.02 mmol N m<sup>-3</sup> on March 1. The  
760 rate of IF grazing on ice algae was calculated following the Ivlev relationship:

$$761 \text{ Grz} = \max \{0, \text{Grz}_{\max} \times (1 - \exp \{ \lambda (\text{IA}^* - \text{IA}) \} ) \},$$

762 where the maximum grazing rate  $Grz_{max}$  of  $0.4 \text{ d}^{-1}$  at  $0 \text{ }^{\circ}\text{C}$ , the Ivlev constant  $\lambda$  of  $1.4 \text{ (mmol N}$   
763  $\text{m}^{-3})^{-1}$ , and the feeding threshold value  $IA^*$  of  $0.04 \text{ mmol N m}^{-3}$  were given, as well as the  
764 grazing of mesozooplankton (ZL) on pelagic diatom (PL) in the original NEMURO model  
765 (Kishi et al., 2007). The Ivlev formulation assumes that no grazing occurs at an ice algal  
766 concentration  $IA$  lower than  $IA^*$ . The modeled ice algal biomass showed the rapid decline after  
767 a similar peak compared with the original case (Fig. 4g). The ice-related fauna gradually  
768 increased following the ice algal bloom. A resultant peak of the IF biomass was  $0.07 \text{ mmol N}$   
769  $\text{m}^{-2}$ . This grazing process slightly contributed to the reduced PON flux (Fig. 14h). After sea ice  
770 melting, the released IF was included in ZL in the water column. For the sake of the enhanced  
771 grazing pressure in the water column, the phytoplankton biomass was also smaller than in the  
772 original case (not shown). We used same parameter values of IF grazing on  $IA$  as those of ZL  
773 on PL. When the skeletal layer is regarded as a refuge for ice algae from potential grazers, the  
774 maximum rate and consequent impact of grazing in the sea ice column should be smaller.

775

### 776 **5.5 Transfer from ice algae to phytoplankton (Case 5)**

777 It has been reported that a part of ice algae exported to the water column could continue  
778 their production activities as phytoplankton and become a zooplankton food source (Michel et  
779 al., 1993; Leventer, 2003; Gradinger et al., 2009). In Case 5, a constant ratio of ice algae  
780 released from the sea ice bottom was included in pelagic diatom (PL). The seeding partition  
781 was set to 0.5, assuming that a half of the released algae behaved in the form of living intact  
782 cells and the residual was included in the ice-related PON. Although the increased PL became a  
783 competitor of ice algae for the uptake of seawater nutrients in the uppermost ocean layer, the  
784 comparison with the original case showed little difference in the ice algal biomass (Figs. 14i).

785 On the other hand, the ice-derived algae staying alive in the water column were eventually  
786 included in the slower-sinking PON produced from pelagic species. These processes  
787 contributed to the decrease in PON flux at the trap depth (Fig. 14j). There is a wide uncertainty  
788 of seeding ratios of the released ice algae. For example, the ratio was set to 0.1 by Jin et al.  
789 (2012). To assess an impact of ice algal seeding to phytoplankton bloom and sinking biogenic  
790 fluxes more accurately, simultaneous measurements of diatom compositions both in the sea ice  
791 and water columns would be necessary.

792

### 793 **5.6 Grazing on ice-derived PON (Case 6)**

794 Zooplankton grazing on sinking biogenic particles could influence the quantity and  
795 composition of export fluxes in the water column. In Case 6, ZL grazing on ice-derived PON  
796 (fPON in the present model) was considered using the Ivlev equation:

$$797 \quad \text{Grz} = \max \{0, \text{Grz}_{\max} \times (1 - \exp\{\lambda (\text{fPON}^* - \text{fPON})\})\},$$

798 where  $\text{Grz}_{\max}$  of  $0.4 \text{ d}^{-1}$  at  $0 \text{ }^{\circ}\text{C}$  and  $\lambda$  of  $1.4 (\text{mmol N m}^{-3})^{-1}$  were given. The feeding threshold  
799 value  $\text{fPON}^*$  was set to zero, and the contributions of other potential grazers (ZS and ZP in the  
800 present model) were neglected, for simplicity. This type of grazing hardly affected the ice algal  
801 biomass as in Case 3 (Fig. 14k), and the PON flux also showed little difference from the  
802 original case (Fig. 14l). A fPON concentration of  $0.5 \text{ } \mu\text{mol N m}^{-3}$  arising in mid-August yielded  
803 a grazing rate Grz of  $2.8 \times 10^{-4} \text{ d}^{-1}$ . As the ZL concentration was still nearly  $50 \text{ } \mu\text{mol N m}^{-3}$  in  
804 the upper 50 m, the grazed amount of fPON was  $0.014 \text{ } \mu\text{mol N m}^{-3} \text{ d}^{-1}$  at the flux peak. The  
805 grazed ratio of  $0.028 \text{ d}^{-1}$  based on the above estimate was an order of magnitude smaller than  
806 the decomposition rate (see Section 5.3). This result indicated that the impact of zooplankton  
807 grazing on ice-derived PON was negligible, at least in the NAP region. In addition, zooplankton

808 would not efficiently capture fast-sinking aggregates as shown in Lake Saroma (Nishi and  
809 Tabeta, 2005). Suspended algae are rather preferable for zooplankton growth (Michel et al.,  
810 1996).  
811



## 812 **6. Summary**

813 Biogeochemical structures in the western Arctic were addressed using a sea ice-ocean  
814 modeling approach. In the present work, a sea ice ecosystem with ice algal activity was newly  
815 incorporated into a pelagic marine ecosystem model. We assumed that ice algae could utilize  
816 nutrients (nitrate, ammonium, and silicate) both in the skeletal layer of sea ice and in the ocean  
817 surface layer (i.e., seawater nutrients). The ratio of the nutrient source varied depending on ice  
818 algal biomass. This “hybrid-type” nutrient uptake formulation is an option to represent more  
819 realistic characteristics of ice algal biology.

820 The modeled ice algal primary production demonstrated noticeable interannual variability  
821 as suggested by previous sediment trap analyses in the NAP region. It was found that year-to-  
822 year changes in ice algal production were closely related to pan-Arctic wind patterns. In winter  
823 2010–2011, strong easterly winds around the Beaufort High induced basin-ward Ekman  
824 transport of shelf-origin surface water and vertical turbulent mixing with underlying nutricline  
825 waters. The higher nitrate concentrations were then distributed in the southern Beaufort Sea and  
826 the Chukchi Borderland. On the other hand, in winter 2011–2012, northwesterly winds  
827 associated with an extension of the Siberian High distributed oligotrophic water from the  
828 central Canada Basin toward the northern Chukchi shelf. Hence, ice algal productivity in the  
829 NAP region was suppressed by a deeper nutricline, in addition to cloud shading of solar  
830 irradiance, until early summer.

831 The modeled summer biogenic particle flux in the NAP region was comparable with the  
832 sediment trap data in 2011 and but was remarkably overestimated in 2012. In summer 2012,  
833 lateral advection processes resulted in the enhanced PON flux, because the ice-ocean flux  
834 exceeded ice algal production in the same location. In August, westerly winds were intensified

835 in the southern part of the cyclone and transported the shelf-origin ice algal patches toward the  
836 NAP region. This cyclone event may have caused the model biases on sea ice motion and  
837 biogenic particle flux. We further addressed several model uncertainties with sensitivity  
838 experiments. The modeled ice algal biomass was highly sensitive to optimum light intensity.  
839 PON flux in the water column varied depending on particle sinking speed in addition to ice  
840 algal productivity. The impacts of various grazing processes on PON flux were relatively minor  
841 within the present cases. However, there still remain more unknown issues on ice algae. For  
842 example, resting spores should be considered for wintering strategy. Successive observations  
843 and model improvements are indispensable to gather ubiquitous findings on ice-related  
844 biological processes.

845

#### 846 **Acknowledgements**

847 This study is supported by the Grant-in-Aid for Scientific Research of Japan Society for the  
848 Promotion of Science (JSPS) (KAKENHI 22221003, 26800248, and 15H01736) and the  
849 GRENE Arctic Climate Change Research Project. Modeling experiments were executed using  
850 the Earth Simulator of Japan Agency for Marine-Science and Technology (JAMSTEC). The  
851 article was much improved by Dr. Nadja Steiner and an anonymous referee.

852

853 **References**

- 854 Aota, M. and Ishikawa, M.: On the extinction coefficient of sea ice, *Low Temperature Science*  
855 *Series A.*, 40, 127–135, 1982.
- 856 Arrigo, K., Kremer, J. N., and Sullivan, C. W.: A simulated Antarctic fast ice ecosystem, *J.*  
857 *Geophys. Res.*, 98, 6929–6946, 1993.
- 858 Arrigo, K. R., Mock T., and Lizotte, M. P.: Primary producers and sea ice. In: Thomas, D. N.,  
859 Dieckmann, G. S. (Eds.), *Sea Ice*. Wiley-Blackwell, Oxford, pp. 283–325, 2010.
- 860 Baker, E. T., Milburn, H. B., and Tennant, D. A.: Field assessment of sediment trap efficiency  
861 under varying flow conditions, *J. Mar. Res.*, 46, 573–592, 1998.
- 862 Bitz, C. M., Holland, M. M., Weaver, A. J., and Eby, M.: Simulating the ice-thickness  
863 distribution in a coupled climate model, *J. Geophys. Res.*, 106, 2441–2463, 2001.
- 864 Bitz, C. M. and Lipscomb, W. H.: An energy-conserving thermodynamic model of sea ice, *J.*  
865 *Geophys. Res.*, 104, 15,669–15,677, 1999.
- 866 Bluhm, B. A., Gradinger, R. R., Schnack-Schiel, S. B.: Sea ice meio- and macro-fauna. In:  
867 Thomas, D. N., Dieckmann, G. S. (Eds.), *Sea Ice*. Wiley-Blackwell, Oxford, pp. 357–393,  
868 2010.
- 869 Boetius, A. et al.: Export of algal biomass from the melting Arctic sea ice, *Science*, 339, 1430–  
870 1432, 2013.
- 871 Cota, G. F., Legendre, L., Gosselin, M., and Ingram, R. G.: Ecology of bottom ice algae: I.  
872 Environmental controls and variability, *J. Mar. Sys.*, 2, 257–277, 1991.
- 873 Cota, G. F. and Smith, R. E. H.: Ecology of bottom ice algae: II. Dynamics, distributions and  
874 productivity, *J. Mar. Sys.*, 2, 279–295, 1991.

875 Cremer, H: Distribution patterns of diatom surface sediment assemblages in the Laptev Sea  
876 (Arctic Ocean). *Mar. Micropal.*, 38, 39–67, 1999.

877 Deal, C., Jin, M., Elliot S., Hunke, E., Maltrud, M., and Jeffery, N.: Large-scale modeling of  
878 primary production and ice algal biomass within arctic sea ice in 1992, *J. Geophys. Res.*,  
879 116, C07004, doi:10.1029/2010JC006409, 2011.

880 Dupont, F.: Impact of sea-ice biology on overall primary production in a biophysical model of  
881 the pan-Arctic Ocean, *J. Geophys. Res.*, 117, C00D17, doi:10.1029/2011JC006983, 2012.

882 Fahl, K. and Nöthig, E.-M.: Lithogenic and biogenic particle fluxes on the Lomonosov Ridge  
883 (central Arctic Ocean) and their relevance for sediment accumulation: Vertical vs. lateral  
884 transport, *Deep Sea Res- I*, 54, 1256–1272, 2007.

885 Forest, A., et al.: Particulate organic carbon fluxes on the slope of the Mackenzie Shelf  
886 (Beaufort Sea): Physical and biological forcing of shelf-basin exchanges. *J. Mar. Sys.*, 68,  
887 39–54, 2007.

888 Garcia, H. E., Locarnini, R. A., Boyer, T. P., Antonov, J. I., Baranova, O. K., Zweng, M. M.,  
889 Reagan, J. R., and Johnson, D. R.: *World Ocean Atlas 2013, Volume 4: Dissolved Inorganic*  
890 *Nutrients (phosphate, nitrate, silicate)*. Levitus, S., Ed., Mishonov, A. Technical Ed.;  
891 NOAA Atlas NESDIS, 76, 25pp., 2013.

892 Gardner, D. H.: The effect of tilt on sediment trap efficiency, *Deep Sea Res.-A*, 32, 349–361,  
893 1985.

894 Gosselin, M., Levasseur, M., Wheeler, P. A., Horner, R. A., and Booth, B. C.: New  
895 measurements of phytoplankton and ice algal production in the Arctic Ocean, *Deep Sea*  
896 *Res.-II*, 44, 1623–1644, 1997.

897 Gradinger, R.: Sea-ice algae: Major contributors to primary production and algal biomass in the  
898 Chukchi and Beaufort Seas during May/June 2002, *Deep Sea Res.-II*, 56, 1201–1212, 2009.

899 Haas, C., Hendricks, S., Eicken, H., and Herber, A.: Synoptic airborne thickness surveys reveal  
900 state of Arctic sea ice cover, *Geophys. Res. Lett.*, 37, L09501, doi:10.1029/2010GL042652,  
901 2010.

902 Hasumi, H.: CCSR Ocean Component Model (COCO) version 4.0, Center for Climate System  
903 Research Report, Univ. of Tokyo, 25, 103pp., 2006.

904 Honda, M. C., Kawakami, H., Watanabe, S., and Saino, T.: Concentration and vertical flux of  
905 Fukushima-derived radiocesium in sinking particles from two sites in the Northwestern  
906 Pacific Ocean, *Biogeosciences*, 10, 3525–3534, doi:10.5194/bg-10-3525-2013, 2013.

907 Honjo, S., et al.: Biological pump processes in the cryopelagic and hemipelagic Arctic Ocean:  
908 Canada Basin and Chukchi Rise, *Prog. Oceanogr.*, 85, 137–170, 2010.

909 Hunke, E. C. and Dukowicz, J. K.: An elastic-viscous-plastic model for sea ice dynamics, *J.*  
910 *Phys. Oceanogr.*, 27, 1849–1867, 1997.

911 Hwang, J., Kim, M., Manganini, S. J., McIntyre, C. P., Haghypour, N., Park, J. J., Krishfield, R.  
912 A., Macdonald, R. W., McLaughlin, F. A., and Eglinton, T. I.: Temporal and spatial  
913 variability of particle transport in the deep Arctic Canada Basin, *J. Geophys. Res.*, 120,  
914 2784–2799, doi:10.1002/2014JC010643, 2015.

915 Ikenoue, T., Bjorklund, K. R., Kruglikova, S. B., Onodera, J., Kimoto, K., and Harada, N.: Flux  
916 variations and vertical distributions of siliceous Rhizaria (Radiolaria and Phaeodaria) in the  
917 western Arctic Ocean: indices of environmental changes, *Biogeosciences*, 12, 2019–2046,  
918 doi:10.5194/bg-12-2019-2015, 2015.

- 919 Jin, M., Deal, C. J., Wang, J., Shin, K.-H., Tanaka, N., Whitledge, T. E., Lee, S. H., Gradinger,  
920 R. R.: Controls of the landfast ice-ocean ecosystem offshore Barrow, Alaska, *Ann. Glaciol.*,  
921 44, 63–72, 2006.
- 922 Jin, M., Deal, C., Lee, S. H., Elliott, S., Hunke, E., Maltrud, and M., Jeffery, N.: Investigation  
923 of Arctic sea ice and ocean primary production for the period 1992-2007 using a 3-D global  
924 ice-ocean ecosystem model, *Deep Sea Res.-II*, 81–84, 28–35,  
925 doi:10.1016/j.dsr2.2011.06.003, 2012.
- 926 Kishi, M. J., et al.: NEMURO—a lower trophic level model for the North Pacific marine  
927 ecosystem, *Ecol. Model.*, 202, 12–25, 2007.
- 928 Lalande, C., Nöthig, E.-M., Somavilla, R., Bauerfeind, E., Shevchenko, V., and Okolodkov, Y.:  
929 Variability in under-ice export fluxes of biogenic matter in the Arctic Ocean, *Global*  
930 *Biogeochem. Cycles*, 28, doi:10.1002/2013GB004735, 2014.
- 931 Lavoie, D., Denman, K., and Michel, C.: Modeling ice algal growth and decline in a seasonally  
932 ice-covered region of the Arctic (Resolute Passage, Canadian Archipelago), *J. Geophys.*  
933 *Res.*, 110, C11009, doi:10.1029/2005JC002922, 2005.
- 934 Lavoie, D., Denman, K. L., and Macdonald, R. W.: Effects of future climate change on primary  
935 productivity and export fluxes in the Beaufort Sea, *J. Geophys. Res.*, 115, C04018,  
936 doi:10.1029/2009JC005493, 2010.
- 937 Leonard, B. P., MacVean, M. K., and Lock, A. P.: The flux-integral method for multi-  
938 dimensional convection and diffusion, NASA Tech. Memo, 106679/ICOMP-94-13, NASA,  
939 Washington, D. C., 1994.
- 940 Leventer, A.: Particulate flux from sea ice in polar waters. In: Thomas, D. N. and Dieckmann G.  
941 S. (Eds.), *Sea Ice*. Wiley-Blackwell, Oxford, pp. 303–332, 2003.

942 Llinas, L., Pickart, R. S., Mathis, J. T., and Smith, S. L.: Deep Sea Res.-II, 56, 1290–1304, 2009.

943 Lipscomb, W. H.: Remapping the thickness distribution in sea ice models, *J. Geophys. Res.*,

944 106, 13,989–14,000, 2001.

945 Matsuno, K., Yamaguchi, A., Fujiwara, A., Onodera, J., Watanabe, E., Harada, N., and Kikuchi,

946 T.: Seasonal changes in the population structure of dominant planktonic copepods collected

947 using a sediment trap moored in the western Arctic Ocean, *J. Natural History*, in press.,

948 2015.

949 McLaughlin, F. A. and Carmack, E. C.: Deepening of the nutricline and chlorophyll maximum

950 in the Canada Basin interior, 2003–2009, *Geophys. Res. Lett.*, 37, L24602,

951 doi:10.1029/2010GL045459, 2010.

952 Michel, C., Legendre, L. L., Therriault, J.-C., Demers, S., and Vandeveld T.: Springtime

953 coupling between ice algal and phytoplankton assemblages in southeastern Hudson Bay,

954 Canadian Arctic, *Polar Biol.*, 13, 441–449, 1993.

955 Michel, C., Legendre, L., Ingram, R. G., Gosselin, M., and Levasseur, M.: Carbon budget of

956 sea-ice algae in spring: Evidence of a significant transfer to zooplankton grazers, *J.*

957 *Geophys. Res.*, 101, 18,345–18,360, 1996.

958 Nishi, Y., and Tabeta, S.: Analysis of the contribution of ice algae to the ice-covered ecosystem

959 in Lake Saroma by means of a coupled ice-ocean ecosystem model. *J. Mar. Sys.*, 55, 249–

960 270, 2005

961 Nishino, S., Kikuchi, T., Yamamoto-Kawai, M., Kawaguchi, Y., Hirawake, T., and Itoh, M.:

962 Enhancement/reduction of biological pump depends on ocean circulation in the sea-ice

963 reduction regions of the Arctic Ocean. *J. Oceanogr.*, 67, 305–314, 2011.

964 Noh, Y. and Kim, H. J.: Simulations of temperature and turbulence structure of the oceanic  
965 boundary layer with the improved near-surface process, *J. Geophys. Res.*, 104, 15,621–  
966 15,634, 1999.

967 Onodera, J., Watanabe, E., Harada, N., and Honda, M. C.: Diatom flux reflects water-mass  
968 conditions on the southern Northwind Abyssal Plain, Arctic Ocean, *Biogeosciences*, 12,  
969 1373–1385, doi:10.5194/bg-12-1373-2015, 2015.

970 Peralta-Ferriz, C. and Woodgate, R. A.: Seasonal and interannual variability of pan-Arctic  
971 surface mixed layer properties from 1979 to 2012 from hydrographic data, and the  
972 dominance of stratification for multiyear mixed layer depth shoaling, *Prog. Oceanogr.*, in  
973 press, doi:10.1016/j.pocean.2014.12.005, 2015.

974 Pogson, L., Tremblay, B., Lavoie, D., Michel, C., and Vancoppenolle, M.: Development and  
975 validation of a one-dimensional snow-ice algae model against observations in Resolute  
976 Passage, Canadian Arctic Archipelago, *J. Geophys. Res.*, 116, C040110,  
977 doi:10.1029/2010JC006119, 2011.

978 Proshutinsky, A. Y. and Johnson, M. A.: Two circulation regimes of the wind-driven Arctic  
979 Ocean, *J. Geophys. Res.*, 102, 12,493–12,514, 1997.

980 Proshutinsky, A., Krishfield, R., Timmermans, M.-L., Toole, J., Carmack, E., McLaughlin, F.,  
981 Williams, W. J., Zimmermann, S., Itoh, M., and Shimada, K.: Beaufort Gyre freshwater  
982 reservoir: State and variability from observations, *J. Geophys. Res.*, 114, C00A10,  
983 doi:10.1029/2008JC005104, 2009.

984 Saha, S., et al.: The NCEP Climate Forecast System reanalysis. *Bull. Am. Meteorol. Soc.*, 91,  
985 1015–1057, doi:10.1175/2010BAMS3001.1, 2010.



- 986 Simmonds, I. and Rudeva, I.: The great Arctic cyclone of August 2012, *Geophys. Res. Lett.*, 39,  
987 L23709, doi:10.1029/2012GL054259, 2012.
- 988 Spall, M. A., Pickart, R. S., Frantantoni, P. S., and Plueddemann, A. J.: Western Arctic  
989 shelfbreak eddies: Formation and transport, *J. Phys. Oceanogr.*, 38, 1644–1668, 2008.
- 990 Steele, M., Morley, R., and Ermold, W.: PHC: A global ocean hydrography with a high-quality  
991 Arctic Ocean, *J. Clim.*, 14, 2079–2087, 2001.
- 992 Tedesco, L., Vichi, M., Haapala, J., and Stipa, T.: A dynamic Biologically Active Layer for  
993 numerical studies of the sea ice ecosystem, *Ocean Model.*, 35, 89–104, 2010.
- 994 Vancoppenolle, M., Goosse, H., de Montety A., Fichefet, T., Tremblay, B., and Tison, J. –L.:  
995 Modeling brine and nutrient dynamics in Antarctic sea ice: The case of dissolved silica, *J.*  
996 *Geophys. Res.*, 115, C02005, doi:10.1029/2009JC005359.
- 997 Wassmann, P.: Arctic marine ecosystems in an era of rapid climate change. *Prog. Oceanogr.* 90,  
998 1–17, 2011.
- 999 Watanabe, E.: Beaufort shelf break eddies and shelf-basin exchange of Pacific summer water in  
1000 the western Arctic Ocean detected by satellite and modeling analyses, *J. Geophys. Res.*,  
1001 116, C08034, doi:10.1029/2010JC006259, 2011.
- 1002 Watanabe, E., Kishi, M. J., Ishida, A., and Aita, M. N.: Western Arctic primary productivity  
1003 regulated by shelf-break warm eddies, *J. Oceanogr.*, 68, 703–718, doi:10.1007/s10872-012-  
1004 0128-6, 2012.
- 1005 Watanabe, E., Onodera, J., Harada, N., Honda, M. C., Kimoto, K., Kikuchi, T., Nishino, S.,  
1006 Matsuno, K., Yamaguchi, A., Ishida, A., and Kishi, M. J.: Enhanced role of eddies in the  
1007 Arctic marine biological pump, *Nature Comm.*, 5, doi:10.1038/ncomms4950, 2014.

1008 Woodgate, R. A., Aagaard, K., and Weingartner, T. J.: Monthly temperature, salinity, and  
1009 transport variability of the Bering Strait through flow, *Geophys. Res. Lett.*, 32, L04601,  
1010 doi:10.1029/2004GL021880, 2005.

1011 Yamazaki, A., Inoue, J., Dethloff, K., Maturilli, M., and König-Langlo, G.: Impact of  
1012 radiosonde observations on forecasting summertime Arctic cyclone formation, *J. Geophys.*  
1013 *Res.*, 120, doi:10.1002/2014JD022925, 2015.

1014 Yang, J.: Seasonal and interannual variability of downwelling in the Beaufort Sea, *J. Geophys.*  
1015 *Res.*, 114, C00A14, doi:10.1029/2008JC005084, 2009.

1016 Zhang, J., Spitz, Y. H., Steele, M., Ashjian, C., Campbell, R., Berline, L., and Matrai, P.:  
1017 Modeling the impact of declining sea ice on the Arctic marine planktonic ecosystem, *J.*  
1018 *Geophys. Res.*, 115, C10015, doi:10.1029/2009JC005387, 2010.

1019 Zhang, J., Lindsay, R., Schweiger, A., and Steele, M.: The impact of an intense summer cyclone  
1020 on 2012 Arctic sea ice retreat, *Geophys. Res. Lett.*, 40, doi:10.1002/grl.50190, 2013.

1021 Zhang, J., Ashjian, C., Campbell, R., Hill, V., Spitz, Y. H., and Steele, M.: The great 2012 Arctic  
1022 Ocean summer cyclone enhanced biological productivity on the shelves, *J. Geophys. Res.*,  
1023 119, 297–312, 2014.

1024 Zhao, M., Timmermans, M.-L., Cole, S., Krishfield, R., Proshutinsky, A., and Toole, J.:  
1025 Characterizing the eddy field in the Arctic Ocean halocline, *J. Geophys. Res.*, 119, 8800–  
1026 8817, doi:10.1002/2014JC010488.

1027

1028 **Table captions**

1029 **Table 1.** Parameters in the sea ice ecosystem model. The values of ice algae are same as those  
1030 of large phytoplankton in the original NEMURO model (Kishi et al., 2007). The PAR fraction  
1031 followed Zhang et al. (2010), and the light extinction rates were derived from Aota and  
1032 Ishikawa (1982). The parameter values of nitrogen and silicon flows in the skeletal layer were  
1033 same as those in the water column, which were also provided by Kishi et al. (2007).

1034

1035 **Table 2.** Monthly mean values of NCEP/CFSR cloud fraction (n. d.), downward shortwave  
1036 radiation ( $\text{W m}^{-2}$ ), 10 m wind speed ( $\text{m s}^{-1}$ ), snow depth (cm), sea ice thickness (cm), and sea  
1037 ice concentration (n. d.) averaged in the NAP region. 2011 (2012) corresponds to the period  
1038 from October 2010 (2011) to September 2011 (2012) to compare the model results.

1039

1040 **Table 3.** Parameters in the sensitivity experiments. Formulations are shown in Section 2.2 and 5.

1041 **Figure captions**

1042 **Figure 1.** Bathymetry of the pan-Arctic sea ice-ocean model COCO. Location of Station NAP  
1043 is indicated by a red dot in the left enlarged view. The NAP region defined in the present study  
1044 is enclosed by  $74^{\circ}$ – $76^{\circ}$ N and  $159^{\circ}$ – $165^{\circ}$ W. The model integration period covers 33 years from  
1045 1979 to 2011 only for the physical oceanographic part using the 25 km resolution version, and  
1046 the obtained fields are given as initial condition for one year experiment from October 2010  
1047 (2011) to September 2011 (2012) in the 2011 (2012) case using the 5 km resolution version  
1048 with marine ecosystem components.

1049

1050 **Figure 2.** Schematic image and configuration of the Arctic NEMURO model. Nitrogen and  
1051 silicon flows are composed of photosynthesis (Photo), shell formation (Shell), respiration (Res),  
1052 excretion (Exc), mortality (Mor), grazing (Grz), predation (Prd), egestion (Ege), decomposition  
1053 (Dec), remineralization (Rem), nitrification (Nit), and sinking (Sink). Ice algal habitat is  
1054 confined to the skeletal layer of sea ice bottom. Ice-related fauna (IF) is calculated only in a  
1055 sensitivity experiment (Case 4). Exchange of biogeochemical variables with the pelagic  
1056 ecosystem is allowed at the ice-ocean interface.

1057

1058 **Figure 3.** Relationships of (a) light extinction rate (non-dimensional (n. d.)) v. s. thickness of  
1059 (dashed line) snow and (solid line) sea ice (cm), (b) light condition term (n. d.) v. s. light  
1060 intensity (PAR) ( $W\ m^{-2}$ ), (c) ice nutrient uptake ratio  $RN_{upSKL}$  (n. d.) v. s. ice algal biomass  
1061 ( $mmol\ N\ m^{-2}$ ), (d) nitrate condition term (n. d.) v. s. nitrate concentration ( $mmol\ N\ m^{-3}$ ), and (e)  
1062 sinking speed of PON derived from (solid line) ice algae and (dashed line) pelagic plankton

1063 groups ( $\text{m d}^{-1}$ ) v. s. depth in the water column (m), respectively, in the Arctic NEMURO model.

1064 See more information in Section 2.2.

1065

1066 **Figure 4.** Seasonal transition of daily mean modeled variables in the NAP region. (a) Sea ice  
1067 concentration (n. d.), (b) sea ice thickness (cm), (c) thermal growth rate of sea ice ( $\text{cm d}^{-1}$ ), (d)  
1068 divergence of sea ice velocity ( $\text{d}^{-1}$ ), (e) Ekman upwelling velocity diagnosed using ocean  
1069 surface stress fields ( $\text{m d}^{-1}$ ), and (f) vertical diffusivity at the depth of 20 m ( $\text{cm}^2 \text{s}^{-1}$ ) in the  
1070 2011 (red line) and 2012 (blue line) cases. Note that negative values in (c), (d), and (e)  
1071 correspond to sea ice melting, convergence of sea ice velocity, and Ekman downwelling,  
1072 respectively. Vertical diffusivity in (f) is shown in a logarithm scale.

1073

1074 **Figure 5.** Modeled annual primary production of ice algae in the (a) 2011 and (b) 2012 cases  
1075 ( $\text{mmol N m}^{-2}$ ). The difference between the two cases is shown in (c). Yellow dots denote the  
1076 location of Station NAP. White dots represent the eastern and western limits of  $75^\circ\text{N}$  section in  
1077 Figs. 6b-c.

1078

1079 **Figure 6.** Modeled seasonal transition of ice algal biomass (a) in the NAP region and (b-c)  
1080 along the  $75^\circ\text{N}$  line ( $\text{mmol N m}^{-2}$ ). Sea floor depths along the east-west section are also plotted  
1081 (m). Red line in (a) and Hovmöller diagram in (b) correspond to the 2011 case. Blue line in (a)  
1082 and the diagram in (c) correspond to the 2012 case. The content of  $1 \text{ mmol N m}^{-2}$  in the sea ice  
1083 column corresponds to the concentration of  $50 \text{ mmol N m}^{-3}$  when the skeletal layer thickness is  
1084 set to 2 cm.

1085

1086 **Figure 7.** Modeled seasonal transition of (a) light intensity (PAR) in the skeletal layer ( $\text{W m}^{-2}$ ),  
1087 (b) light condition term (n. d.), (c) ice nutrient uptake ratio  $\text{RN}_{\text{upSKL}}$  (n. d.), and (d) nitrate  
1088 condition term (n. d.) in the NAP region in the 2011 (red line) and 2012 (blue line) cases. Each  
1089 term in (b-d) corresponds to ice algal value. In (d), the condition terms in the (thick lines)  
1090 skeletal layer and (thin lines) ocean surface layer are shown.

1091

1092 **Figure 8.** Modeled seasonal transition of nitrate concentration (a) in the skeletal layer ( $\text{mmol N}$   
1093  $\text{m}^{-2}$ ) and (b-c) in the top 100 m of water columns ( $\text{mmol N m}^{-3}$ ). Red line in (a) and vertical  
1094 profile in (b) correspond to the 2011 case. Blue line in (a) and the profile in (c) correspond to  
1095 the 2012 case.

1096

1097 **Figure 9.** Modeled (a-b) primary production rate of ice algae and (c-d) PON flux in the NAP  
1098 region in the (a, c) 2011 and (b, d) 2012 cases ( $\mu\text{mol N m}^{-2} \text{d}^{-1}$ ). In (a-b), the daily rate of total  
1099 primary production (black lines) and those derived from nutrients in the skeletal layer (light  
1100 blue lines) and water column (purple lines) are shown. The export flux of PON from the sea ice  
1101 bottom to the underlying water column is overlaid by olive lines. In (c-d), the total simulated  
1102 (black lines) and observed (gray bars) PON fluxes at 180 m are compared. The fluxes  
1103 originating from ice algae (green lines) and pelagic plankton groups (orange lines) are also  
1104 shown.

1105

1106 **Figure 10.** (a-b) (contours) Sea level pressure (SLP) (hPa) and (vectors) wind stress averaged  
1107 (a) from November 2010 to January 2011 and (b) from November 2011 to January 2012. SLP is  
1108 obtained from the NCEP/CFSR dataset, and wind stress vectors are calculated from the SLP  
1109 field using the AOMIP formulation. Unit vector of wind stress is 0.1 Pa. Direction of (c-d)  
1110 satellite-based and (e-f) modeled sea ice velocity in the NAP region (degree). Only daily  
1111 averages whose velocity exceeded  $5 \text{ cm s}^{-1}$  in the (c, e) 2011 and (d, f) 2012 periods are plotted.  
1112 Positive (negative) values of the direction correspond to northward (southward), and solid  
1113 (dashed) bars indicate westward (eastward) motions, respectively. For example, a solid bar of  
1114  $-45^\circ$  means southwestward direction of  $225^\circ$ T.

1115

1116 **Figure 11.** Modeled nitrate concentration ( $\text{mmol N m}^{-3}$ ). The daily mean fields averaged in the  
1117 top 30 m of water columns on March 1 in the (a) 2011 and (b) 2012 cases are shown in the  
1118 upper panels. In these experiments, a passive tracer is provided from the ocean surface to sea  
1119 floor of 100–200 m depth along shelf-basin boundary sandwiched by white contours. Black  
1120 contours correspond to a tracer value of 0.2 (0–30 m average). Orange lines denote the isobaths  
1121 of 1,000 and 3,000 m. The vertical profile in the NAP region on (black) October 1, (blue)  
1122 December 1, and (magenta) February 1 in the (c) 2011 and (d) 2012 cases are shown in the  
1123 lower panels.

1124

1125 **Figure 12.** (a) NCEP/CFSR (contours) sea level pressure (hPa) and (shade) sea ice  
1126 concentration (n. d.) on August 6, 2012. (b) Modeled (contours) PON flux at the depth of 180 m  
1127 and (vectors) sea ice motion averaged for August 3–10 in the 2012 case. The flux contours of 5,  
1128 10, and  $20 \mu\text{mol N m}^2 \text{ d}^{-1}$  are shown around the Chukchi Borderland. The sea ice motion is

1129 overlaid every ten grid (i.e., approximately 50 km), and its unit vector is  $20 \text{ cm s}^{-1}$ . Red dots  
1130 denote the location of Station NAP. August time series of the modeled (c) ice algal biomass  
1131 ( $\text{mmol N m}^{-2}$ ) and (d) PON flux ( $\mu\text{mol N m}^{-2} \text{ d}^{-1}$ ) in the 2012 case (black lines) and the no ice  
1132 algal activity case (blue lines).

1133

1134 **Figure 13.** Schematic image of sensitivity experiments. In Case 4, the grazing pressure of ice-  
1135 related fauna (IF) on ice algae (IA) and the transition from IF to mesozooplankton (ZL) after  
1136 sea ice melting were calculated for the seeding. In Case 5, a part of IA was treated as large  
1137 phytoplankton (PL) after sea ice melting. In Case 6, the ZL grazing on fast-sinking Particulate  
1138 Organic Nitrogen (fPON) was calculated in the water column, and the formulation of slow-  
1139 sinking one (sPON) was not changed.

1140

1141 **Figure 14.** Modeled seasonal transition of (a, c, e, g, i, k) ice algal biomass ( $\text{mmol N m}^{-2}$ ) and  
1142 (b, d, f, h, j, l) PON flux ( $\mu\text{mol N m}^{-2} \text{ d}^{-1}$ ) in the NAP region in (a-b) Case 1, (c-d) Case 2, (e-f)  
1143 Case 3, (g-h) Case 4, (i-j) Case 5, and (k-l) Case 6. Black thin lines correspond to the original  
1144 2011 case. The results with  $I_{\text{opti}}$  of 5 (20)  $\text{W m}^{-2}$  in Case 1,  $\text{KN}_{\text{upSKL}}$  of 0.5 (1.5)  $\text{mmol N m}^{-2}$  in  
1145 Case 2, PON sinking speed of 200 (20)  $\text{m d}^{-1}$  in Case 3 are shown by magenta (blue) lines,  
1146 respectively. The biomass of ice-related fauna is shown by an olive line in Case 4.



Table 1

Parameter	Definition	Value	Unit
<b>[Ice algae]</b>			
$V_{\max}$	Maximum photosynthetic rate at 0 °C	0.8	$d^{-1}$
$K_{NO_3}$	Half saturation constant for nitrate	3.0	$mmol-N m^{-3}$
$K_{NH_4}$	Half saturation constant for ammonium	0.1	$mmol-N m^{-3}$
$K_{SIL}$	Half saturation constant for silicate	6.0	$mmol-N m^{-3}$
$\Psi_{NH_4}$	Ammonium inhibition coefficient	1.5	$(mmol-N m^{-3})^{-1}$
$KN_{upSKL}$	Threshold value of ice/water nutrient uptake	1.0	$mmol-N m^{-2}$
$K_{Gpp}$	Temperature coefficient for photosynthetic rate	0.0693	$^{\circ}C^{-1}$
$I_{opt}$	Optimum light intensity	10	$W m^{-2}$
$Res_0$	Respiration rate at 0 °C	0.03	$d^{-1}$
$K_{Res}$	Temperature coefficient for respiration rate	0.0519	$^{\circ}C^{-1}$
$\gamma$	Extracellular excretion ratio to photosynthesis	0.135	n. d.
$Mor_0$	Mortality rate at 0 °C	0.029	$(mmol-N m^{-3})^{-1} d^{-1}$
$K_{Mor}$	Temperature coefficient for mortality rate	0.0693	$^{\circ}C^{-1}$
$R_{SiN}$	Si:N ratio	2.0	n. d.
$V_{fPONmin}$	Minimum sinking speed of ice-derived PON	50	$m d^{-1}$
<b>[Light property]</b>			
$PAR_{frac}$	Fraction of PAR to shortwave radiation	0.43	n. d.
$k_{snow}$	light extinction rate for snow	0.12	$cm^{-1}$
$k_{ice}$	light extinction rate for sea ice	0.045	$cm^{-1}$
<b>[Nitrogen/Silicon flow]</b>			
$Nit_0$	Nitrification rate at 0 °C	0.03	$d^{-1}$
$K_{Nit}$	Temperature coefficient for nitrification	0.0693	$^{\circ}C^{-1}$
$VP2N_0$	Decomposition rate from PON to ammonium at 0 °C	0.1	$d^{-1}$
$VP2D_0$	Decomposition rate from PON to DON at 0 °C	0.1	$d^{-1}$
$VD2N_0$	Decomposition rate from DON to ammonium at 0 °C	0.02	$d^{-1}$
$VP2Si_0$	Decomposition rate from opal to silicate at 0 °C	0.1	$d^{-1}$
$K_{P2N}/K_{P2D}/K_{D2N}/K_{P2Si}$	Temperature coefficient for decomposition rate	0.0693	$^{\circ}C^{-1}$

Table 2

		Oct	Nov	Dec	Jan	Feb	Mar	Apr	May	Jun	Jul	Aug	Sep
<b>Cloud Fraction</b>	<b>2011</b>	0.98	0.87	0.79	0.79	0.91	0.88	0.72	0.90	0.76	0.92	0.98	0.96
	<b>2012</b>	0.94	0.90	0.67	0.81	0.79	0.56	0.61	0.83	0.88	0.97	0.97	0.96
<b>Shortwave Radiation</b>	<b>2011</b>	9	0	0	0	4	51	165	236	305	217	102	45
	<b>2012</b>	10	0	0	0	4	62	170	245	264	184	92	46
<b>Wind Speed</b>	<b>2011</b>	6.7	5.1	5.0	5.1	6.0	4.3	4.6	4.4	4.5	4.4	5.3	5.4
	<b>2012</b>	8.1	5.0	4.8	5.1	4.7	4.5	4.1	3.9	4.7	4.7	7.1	7.1
<b>Snow Depth</b>	<b>2011</b>	11	23	32	37	41	44	46	33	0	0	0	0
	<b>2012</b>	8	23	22	21	23	23	22	13	0	0	0	0
<b>Sea Ice Thickness</b>	<b>2011</b>	60	209	216	261	276	281	268	249	228	169	78	0
	<b>2012</b>	60	210	232	271	279	278	286	259	207	141	62	0
<b>Sea Ice Concentration</b>	<b>2011</b>	0.21	0.89	0.98	0.99	0.99	0.99	0.99	0.99	0.99	0.83	0.19	0
	<b>2012</b>	0.19	0.90	0.98	0.98	0.98	0.98	0.99	0.97	0.87	0.70	0.18	0

**Table 3**

Parameter	Definition	Value	Unit
[Case 1-1] $I_{opt}$	Optimum light intensity	5	$W m^{-2}$
[Case 1-2] $I_{opt}$	Optimum light intensity	20	$W m^{-2}$
[Case 2-1] $KN_{upSKL}$	Threshold value of ice/water nutrient uptake	1.5	$mmol-N m^{-2}$
[Case 2-2] $KN_{upSKL}$	Threshold value of ice/water nutrient uptake	0.5	$mmol-N m^{-2}$
[Case 3-1] $V_{fPONmin}$	Minimum sinking speed of ice-derived PON	200	$m d^{-1}$
[Case 3-2] $V_{fPONmin}$	Minimum sinking speed of ice-derived PON	20	$m d^{-1}$
[Case 4] $Grz_{max}$ $\lambda$ $IA^*$ $K_{Grz}$	Maximum rate of IF grazing on IA at 0 °C Ivlev constant Feeding threshold value Temperature coefficient for nitrification	0.4 1.4 0.04 0.0693	$d^{-1}$ $(mmol-N m^{-3})^{-1}$ $mmol-N m^{-3}$ $^{\circ}C^{-1}$
[Case 5] $R_{IA2PL}$	Ratio of seeding from IA to PL	0.5	n. d.
[Case 6] $Grz_{max}$ $\lambda$ $fPON^*$ $K_{Grz}$	Maximum rate of ZL grazing on ice-derived PON at 0 °C Ivlev constant Feeding threshold value Temperature coefficient for nitrification	0.4 1.4 0 0.0693	$d^{-1}$ $(mmol-N m^{-3})^{-1}$ $mmol-N m^{-3}$ $^{\circ}C^{-1}$

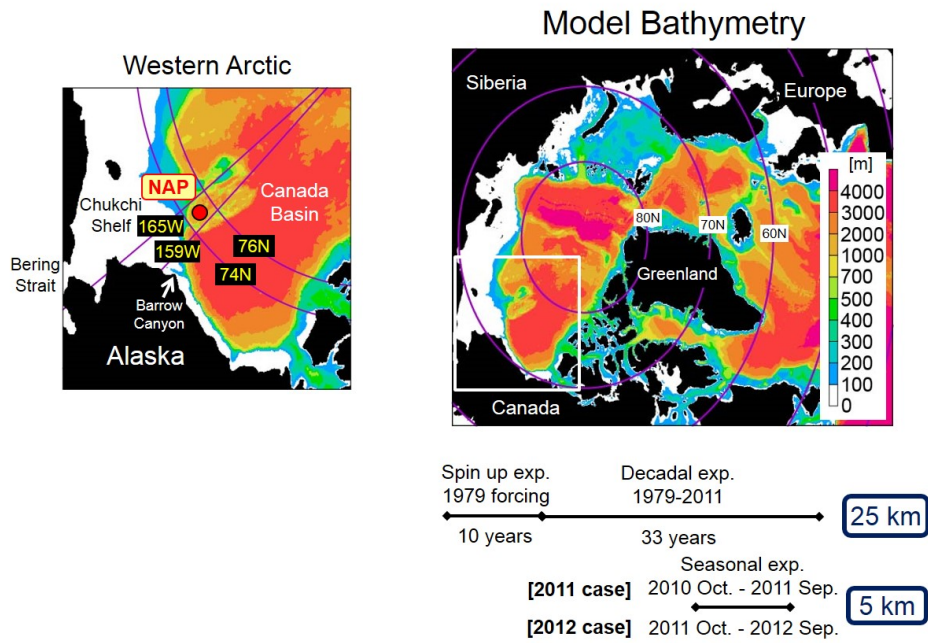


Fig. 1.

C4317

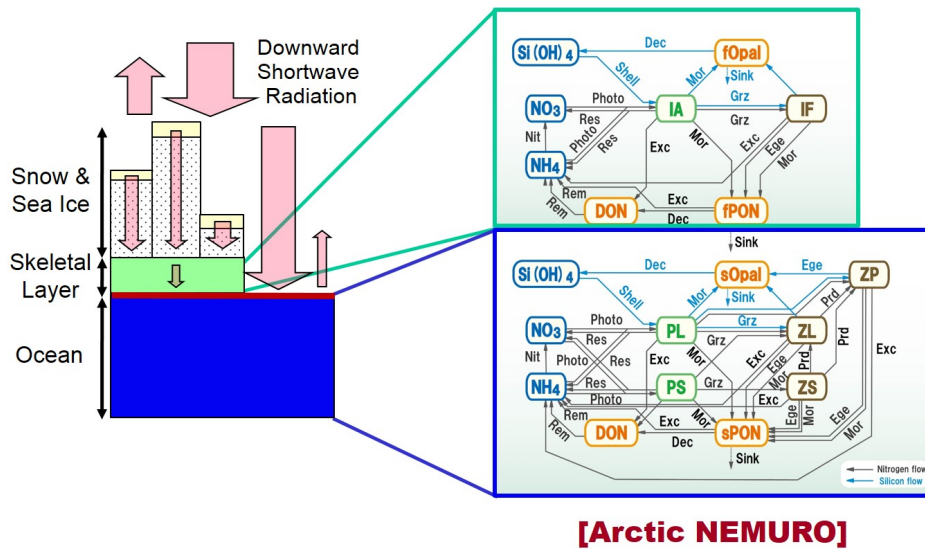


Fig. 2.

C4318

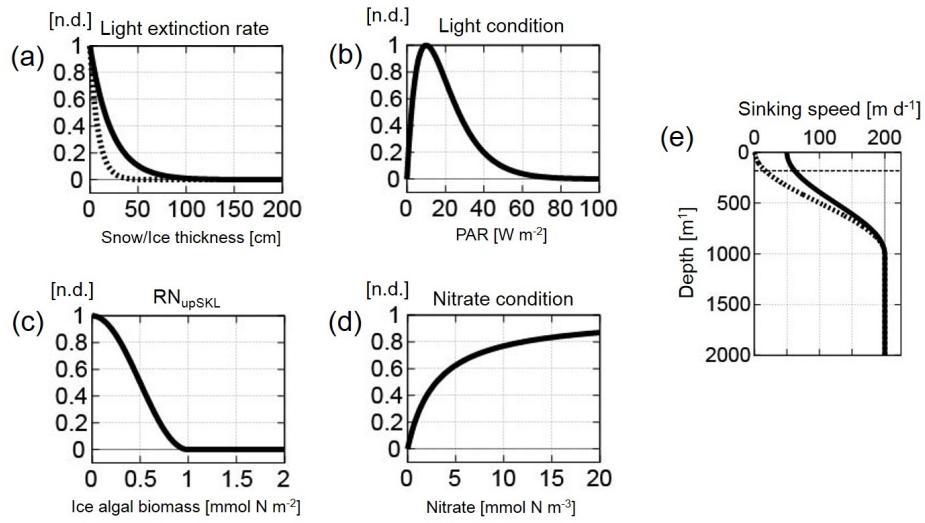


Fig. 3.

C4319

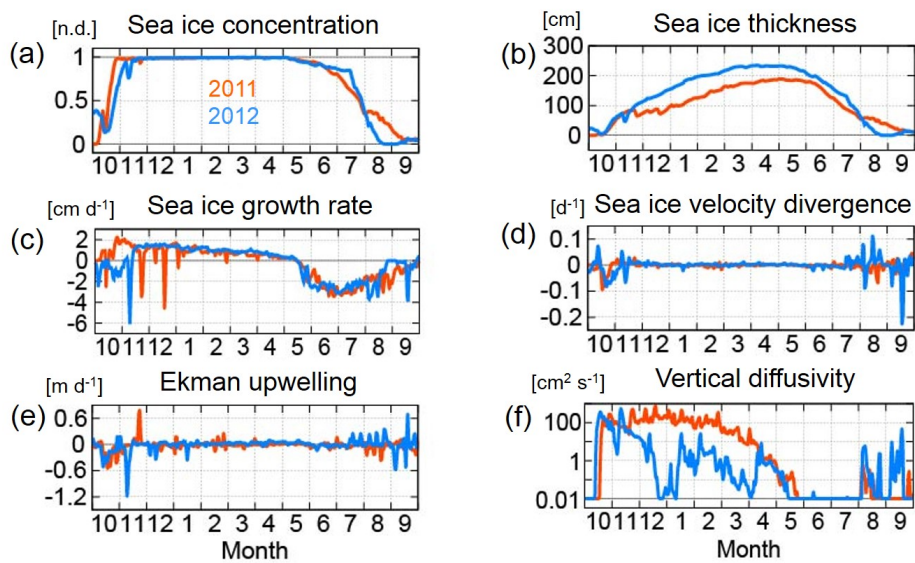


Fig. 4.

C4320

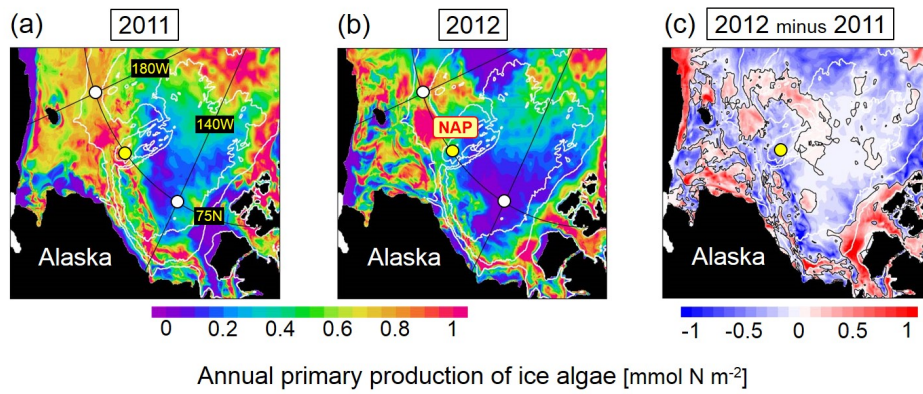


Fig. 5.

C4321

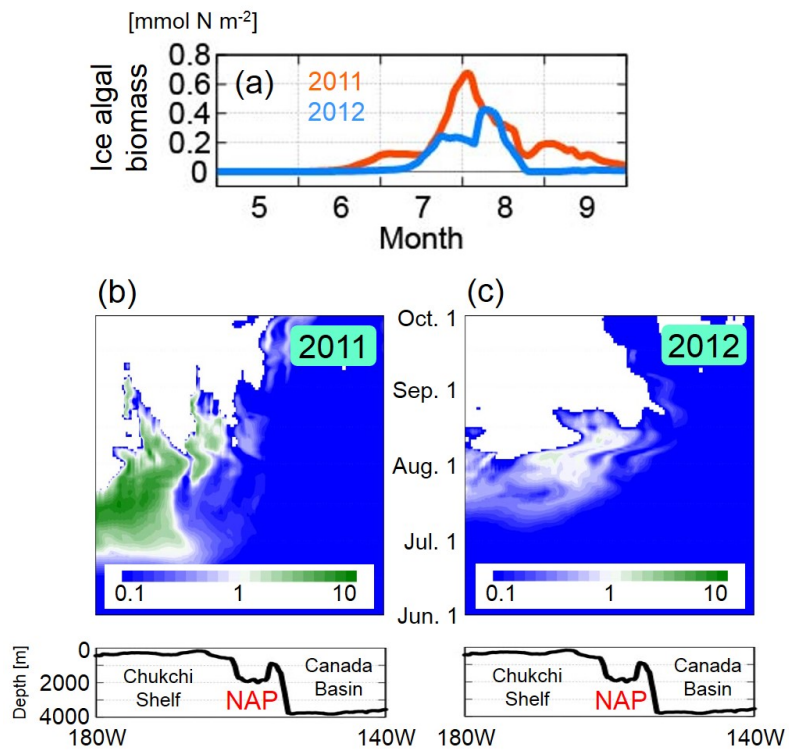


Fig. 6.

C4322

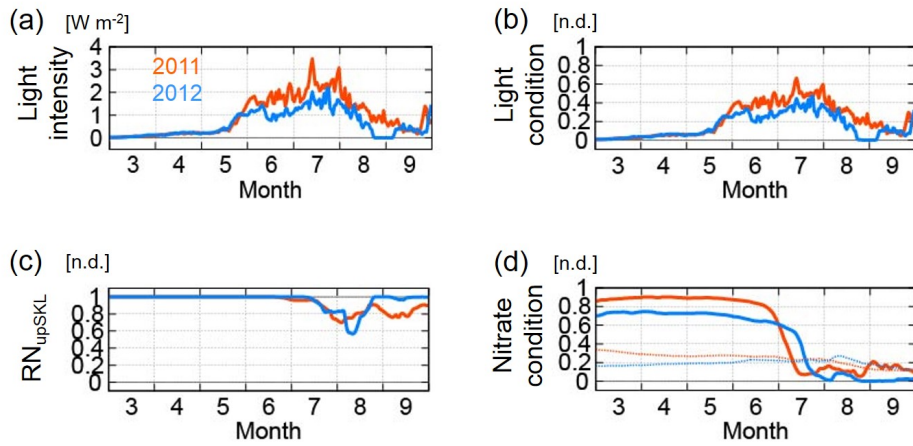


Fig. 7.

C4323

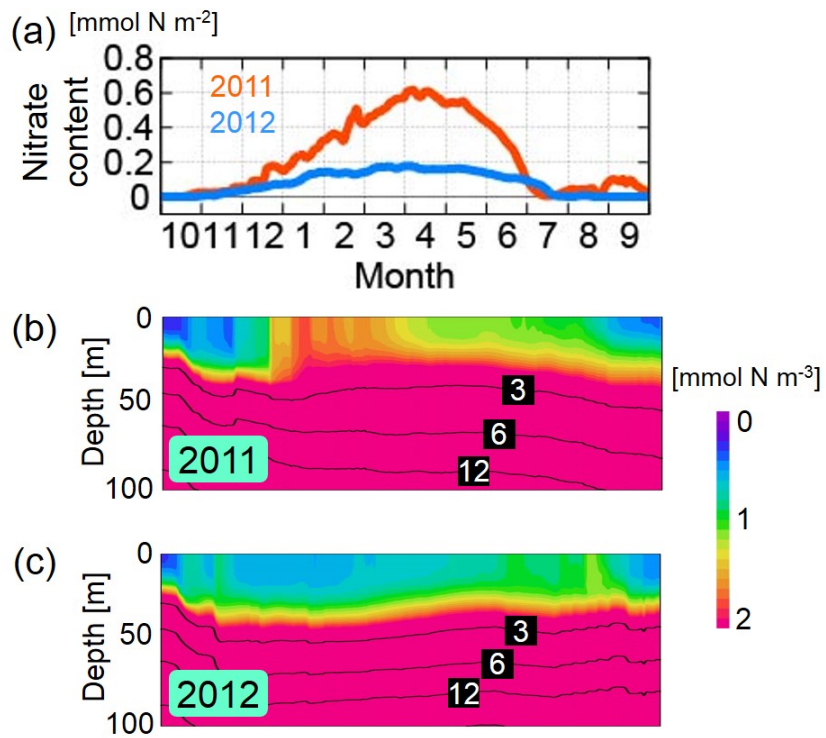


Fig. 8.

C4324

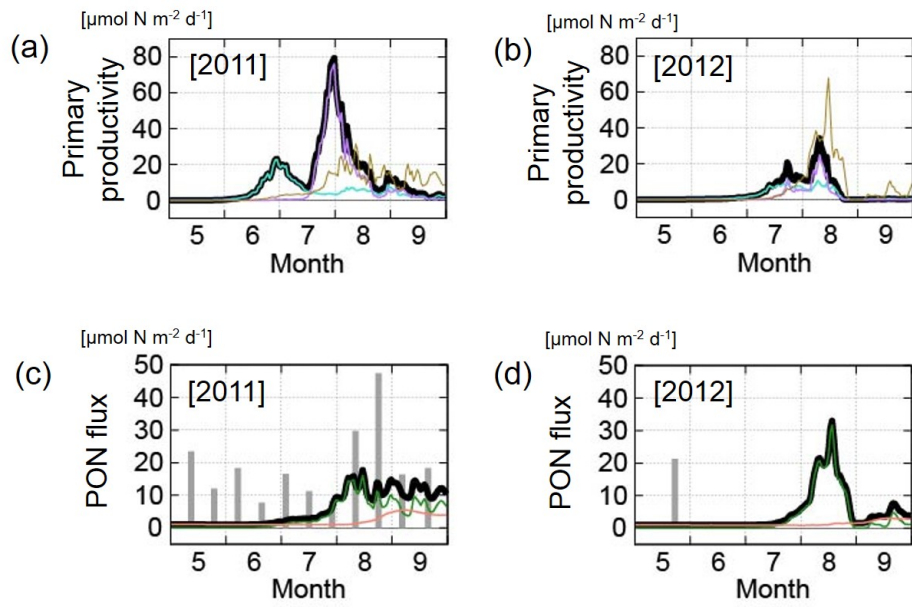


Fig. 9.

C4325

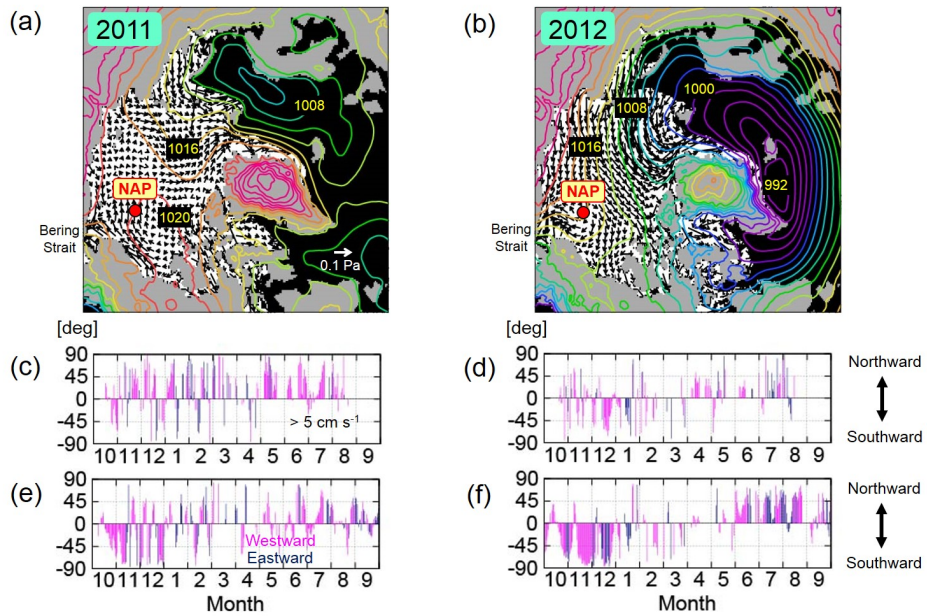


Fig. 10.

C4326



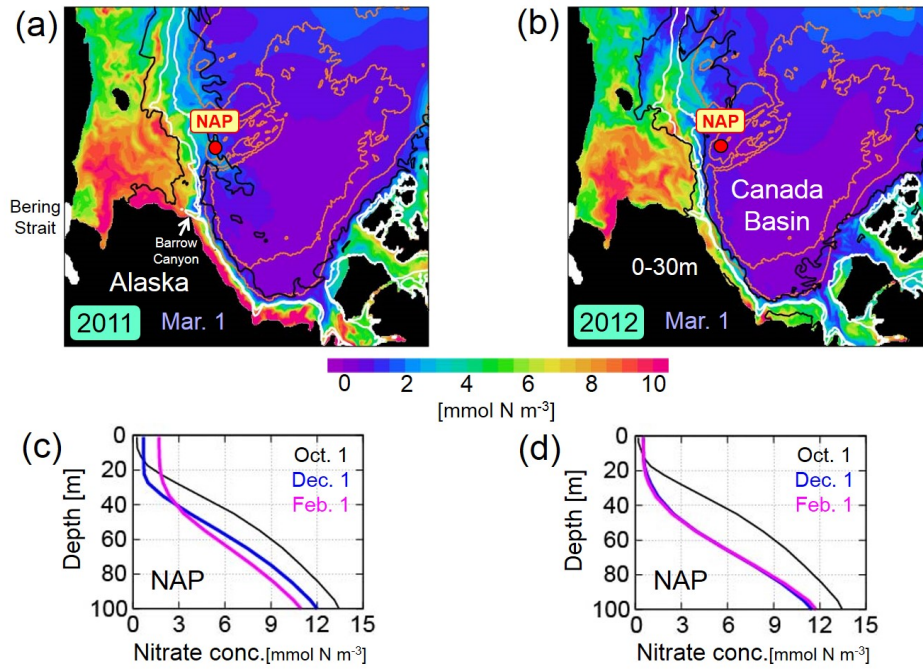


Fig. 11.

C4327

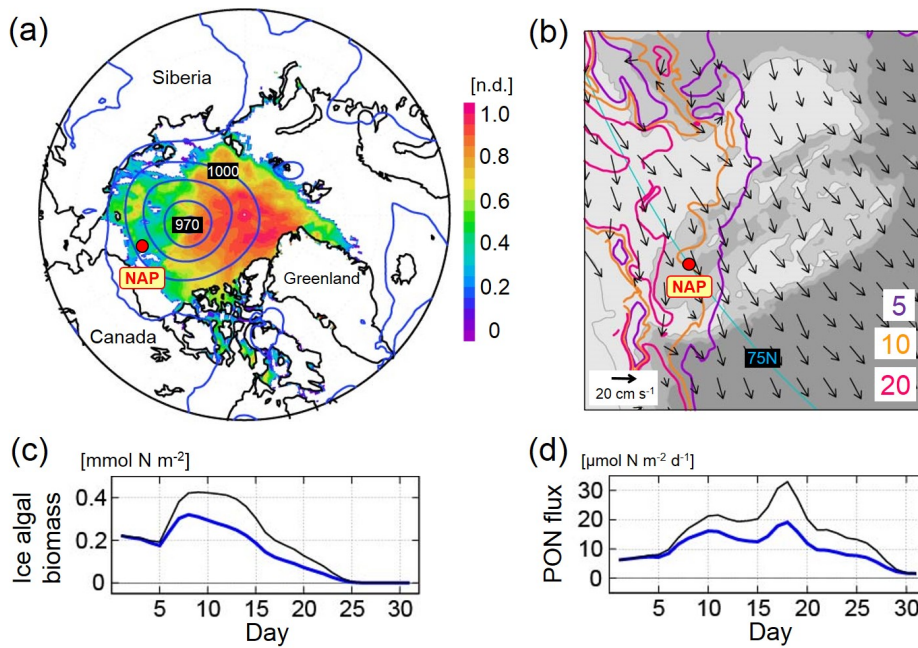


Fig. 12.

C4328

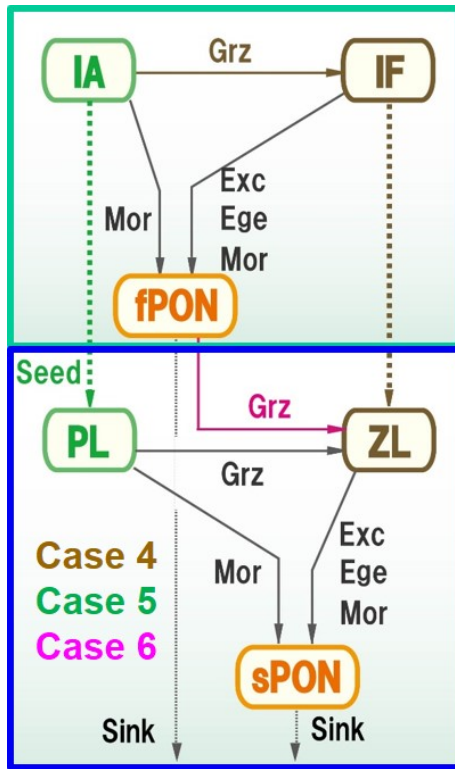


Fig. 13.

C4329

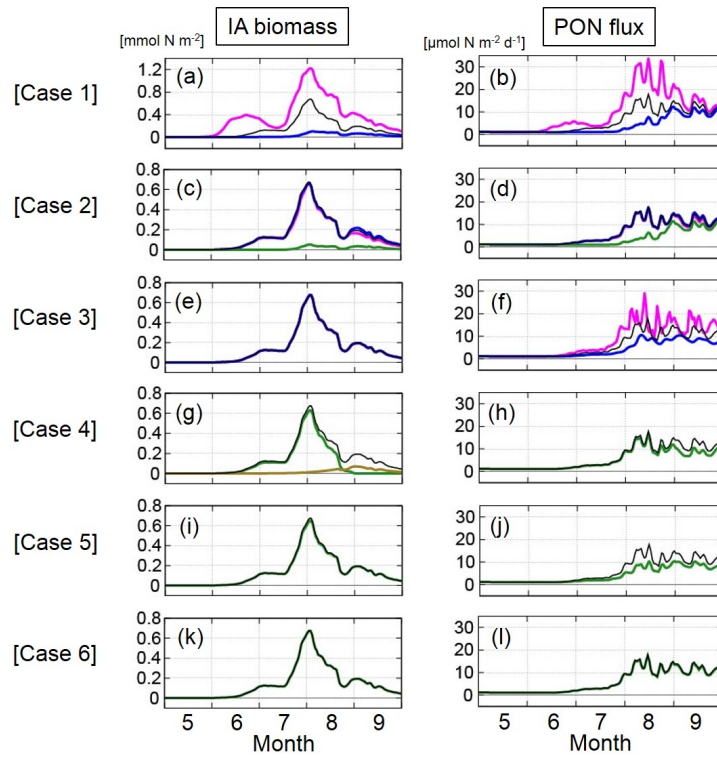


Fig. 14.

C4330